Fractional relaxation noises, motions and the fractional energy balance equation

Shaun Lovejoy
Physics, McGill University,
3600 University st.
Montreal, Que. H3A 2T8
Canada

Abstract:

We consider the statistical properties of solutions of the stochastic fractional relaxation equation and its fractionally integrated extensions that are models for the Earth's energy balance. In these equations, the highest order derivative term is fractional and models the energy storage processes that are scaling over a wide range. When driven stochastically, the system is a Fractional Langevin Equation (FLE) that has been considered in the context of random walks where it yields highly nonstationary behaviour. An important difference with the usual applications it that we instead, consider the stationary solutions of the Weyl fractional relaxation equations whose domain is $-\infty$ to t rather than 0 to t.

An additional key difference is that unlike the (usual) FLEs - where the highest order term is of integer order and the fractional term represents a scaling damping - in the fractional relaxation equation, the highest order derivative term is fractional. When its order is less than ½ - the main empirically relevant range – the solutions are noises (generalized functions) whose high frequency limits are fractional Gaussian noises (fGn). In order to yield physical processes, they must be smoothed and this is conveniently done by considering their integrals. Whereas the basic processes are (stationary) fractional relaxation noises (fRn), their integrals are (nonstationary) fractional Relaxation motions (fRm) that generalize fractional Brownian motion, (fBm).

Since these processes are Gaussian, their properties are determined by their second order statistics; using Fourier and Laplace techniques, we analytically develop corresponding power series expansions for fRn, fRm and their fractionally integrated extensions needed to model energy storage processes. We show extensive analytic and numerical results on the autocorrelation functions, Haar fluctuations and spectra. We display sample realizations.

Finally, we discuss the predictability of these processes which – due to long memories - is a *past* value problem, not an *initial* value problem (that is used for example in highly skillful monthly and seasonal temperature forecasts). We develop an analytic formulae for the fRn forecast skills and compare it to fGn skill. The large scale white noise and fGn limits are attained in a slow power law manner so that when the temporal resolution of the series is small compared to the relaxation time (of the order of a few years in the Earth), fRn and its extensions can mimic a long memory process with a range of exponents wider than possible with fGn or fBm. We discuss the implications for monthly,

42 seasonal, annual forecasts of the Earth's temperature as well as for projecting the
43 temperature to 2050 and 2100.

1. Introduction:

45   Over the last decades, stochastic approaches have rapidly developed and have spread
46 throughout the geosciences.   From early beginnings in hydrology and turbulence,
47 stochasticity has made inroads in many traditionally deterministic areas. This is notably
48 illustrated by stochastic parametrisations of Numerical Weather Prediction models, e.g.
49 [*Buizza et al.*, 1999], and the "random" extensions of dynamical systems theory, e.g.
50 [*Chekroun et al.*, 2010].
51   In parallel, pure stochastic approaches have developed primarily along two distinct
52 lines. One is the classical (integer ordered) stochastic differential equation approach based
53 on the Itô or Stratonivch calculii that goes back to the 1950's (see the useful review
54 [*Dijkstra*, 2013]). The other is the scaling strand that encompasses both linear (monofractal,
55 [*Mandelbrot*, 1982]) and nonlinear (multifractal) models (see the review [*Lovejoy and*
56 *Schertzer*, 2013]) that are based on phenomenological scaling models, notably cascade
57 processes. These and other stochastic approaches have played important roles in nonlinear
58 Geoscience.
59   Up until now, the scaling and differential equation strands of stochasticity have had
60 surprisingly little overlap.   This is at least partly for technical reasons: integer ordered
61 stochastic differential equations have exponential Green's functions that are incompatible
62 with wide range scaling. However, this shortcoming can – at least in principle - be easily
63 overcome by introducing at least some derivatives of fractional order. Once the (typically)
64 ad hoc restriction to integer orders is dropped, the Green's functions are based on
65 "generalized exponentials" that are in turn based on fractional powers (see the review
66 [*Podlubny*, 1999]).   The integer-ordered stochastic equations that have received most
67 attention are thus the exceptional, nonscaling special cases. In physics they correspond to
68 classical Langevin equations; in geophysics and climate modelling, they correspond to the
69 Linear Inverse Modelling (LIM) approach that goes back to [*Hasselmann*, 1976] later
70 elaborated notably by [*Penland and Magorian*, 1993], [*Penland*, 1996], [*Sardeshmukh et*
71 *al.*, 2000], [*Sardeshmukh and Sura*, 2009] and [*Newman*, 2013]. Although LIM is not the
72 only stochastic approach to climate, in two recent representative multi-author collections
73 ([*Palmer and Williams*, 2010] and [*Franzke and O'Kane*, 2017]), all 32 papers shared the
74 integer ordered assumption (a single exception being [*Watkins*, 2017], see also [*Watkins*
75 *et al.*, 2020]).
76   Under the title "Fractal operators" [*West et al.*, 2003], reviews and emphasizes that
77 in order to yield scaling behaviours, it suffices that stochastic differential equations contain
78 fractional derivatives. However, when it is the time derivatives of stochastic variables that
79 are fractional - fractional Langevin equations (FLE) - then the relevant processes are
80 generally non-Markovian [*Jumarie*, 1993], so that there is no Fokker-Planck (FP) equation
81 describing the corresponding probabilities. Even in the relatively few cases where the FLE
82 has been studied, the fractional terms are generally models of viscous damping so that the
83 highest order terms are still integer ordered (an exception is [*Watkins et al.*, 2020] who
84 mentions "fractionally integrated FLE" of the type studied here but without investigating
85 its properties). Integer ordered terms have the convenient consequence of regularizing the

86   solutions so that they are at least root mean square continuous; in this paper the highest
87   order derivatives are fractional so that when the highest order terms are ≤1/2, the solutions
88   are "noises" i.e. generalized functions that must be smoothed in order to represent
89   physically meaningful quantities.
90   An additional obstacle is that - as with the simplest scaling stochastic model –
91   fractional Brownian motion (fBm, [*Mandelbrot and Van Ness*, 1968]) - we expect that the
92   solutions will not be semi-martingales and hence that the Itô calculus used for integer
93   ordered equations will not be applicable (see [*Biagini et al.*, 2008]). This may explain the
94   relative paucity of mathematical literature on stochastic fractional equations (see however
95   [*Karczewska and Lizama*, 2009]). In statistical physics, starting with [*Mainardi and Pironi*,
96   1996], [*Metzler and Klafter*, 2000], [*Lutz*, 2001] and helped with numerics, the FLE (and
97   a more general "Generalized Langevin Equation" [*Kou and Sunney Xie*, 2004], [*Watkins
98   et al.*, 2019]) has received a little more attention as a model for (nonstationary) particle
99   diffusion (see [*West et al.*, 2003] for an introduction, or [*Vojta et al.*, 2019] for a more
100   recent example). These technical aspects may explain why the statistics of the resulting
101   processes are not available in the literature.
102   Technical difficulties may also explain the apparent paradox of Continuous Time
103   Random Walks (CTRW) and other approaches to anomalous diffusion that involve
104   fractional equations. While CTRW probabilities are governed by the deterministic
105   fractional ordered Generalized Fractional Diffusion equation (e.g. [*Hilfer*, 2000], [*Coffey
106   et al.*, 2012]), the walks themselves are based on specific particle jump models rather than
107   (stochastic) Langevin equations. Alternatively, a (spatially) fractional ordered Fokker-
108   Planck equation may be derived from an integer-ordered but nonlinear Langevin equation
109   for a diffusing particle driven by an (infinite variance) Levy motion [*Schertzer et al.*, 2001].
110   In nonlinear geoscience, it is all too common for mathematical models and techniques
111   developed primarily for mathematical reasons, to be subsequently applied to the real world.
112   This approach - effectively starting with a solution and then looking for a problem -
113   occasionally succeeds, yet historically the converse has generally proved more fruitful.
114   The proposal that an understanding of the Earth's energy balance requires the Fractional
115   Energy Balance Equation (FEBE, [*Lovejoy et al.*, 2021], announced in [*Lovejoy*, 2019a])
116   is an example of the latter. First, the scaling exponent of macroweather (monthly, seasonal,
117   interannual) temperature stochastic variability was determined ($H_I \approx$ -0.085±0.02) and
118   shown to permit skillful global temperature predictions, [*Lovejoy*, 2015b], [*Lovejoy et al.*,
119   2015], [*Del Rio Amador and Lovejoy*, 2019], and then it was extended to regional
120   temperatures (at 2°x2° resolution) [*Del Rio Amador and Lovejoy*, 2019; *Del Rio Amador
121   and Lovejoy*, 2021a; *Del Rio Amador and Lovejoy*, 2021b]. The latter papers showed how
122   the long memory high frequency approximation to the FEBE can not only make state of
123   the art multi-month temperature forecasts, but the corresponding simulations generate
124   emergent properties such as realistic El Nino events.
125   In parallel, the multidecadal deterministic response to external (anthropogenic,
126   deterministic) forcing was shown to also obey a scaling law but with a different exponent
127   [*Hebert*, 2017], [*Lovejoy et al.*, 2017], [*Procyk et al.*, 2020] ($H_F \approx$ -0.5±0.2). It was only
128   then was realized that the order h FEBE naturally accounts for both the high and low
129   frequency global temperature exponents with $h = H_I + 1/2$ and $H_F = -h$ with both empirical
130   exponents recovered with a FEBE of order $h \approx 0.42$±0.02. The realization that the FEBE

131   fit these basic empirical facts motivated the present research into its statistical properties
132   including its predictability.
133   In the EBE, energy storage is modelled by a uniform slab of material implying that
134   when perturbed, the temperature exponentially relaxes to a new thermodynamic
135   equilibrium. However, as reviewed in [*Lovejoy and Schertzer*, 2013]), both conventional
136   Global Circulation Models and observations show that atmospheric, oceanic and surface
137   (e.g. topographic) structures are spatially scaling. A consequence is that the temperature
138   relaxes to equilibrium in a power law manner. This motivated earlier approaches ([*van
139   Hateren*, 2013], [*Rypdal*, 2012], [*Hebert*, 2017], [*Lovejoy et al.*, 2017]) to postulate that
140   the climate response function (CRF) itself is scaling. However, these models require either
141   ad hoc truncations or imply infinite sensitivity to small pertubations [*Rypdal*, 2015].
142   The FEBE instead situates the scaling in the energy storage processes; this is the
143   physical basis for the phenomenological derivation of the FEBE proposed in [*Lovejoy et
144   al.*, 2021] and the zeroth order term determines guarantees that equilibrium is reached after
145   long enough times.   The scaling of the basic physical quantities in both time and space
146   motivates the study of the FEBE and its fractionally integrated extensions discussed below
147   temperature treated as a stochastic variable. The FEBE determines the Earth's global
148   temperature when the energy storage processes are scaling and modelled by a fractional
149   time derivative term. Recently, analysis of the atmospheric radiation budget has shown
150   that at least over some regions, the internal component of the radiative forcing may itself
151   be scaling, this justifies the consideration of the extensions to fGn forcing.
152   The FEBE differs from the classical energy balance equation (EBE) in several ways.
153   Whereas the EBE is integer ordered and describes the deterministic, exponential relaxation
154   of the Earth's temperature to equilibrium, the FEBE is of fractional order and because it is
155   both deterministic and stochastic it unites all the forcings and responses into a single model.
156   Whereas the former represents the forcing and response to the unresolved degrees of
157   freedom - the "internal variability" - and is treated as a zero mean Gaussian noise, the latter
158   represents the external (e.g. anthropogenic) forcing and the forced response modelled by
159   the (deterministic) total external forcing. Complementary work [*Procyk et al.*, 2020] uses
160   the deterministic FEBE as the basic model for the response to external forcing, but it uses
161   Bayesian parameter estimation that uses the stochastic FEBE to characterize the likelihood
162   function of the residuals assumed to be the responses to stochastic internal forcing and
163   governed by the same equation. It thus avoids the ad hoc error models involved in
164   conventional Bayesian parameter estimation. The result is a parsimonious, FEBE
165   projection of the Earth's temperature to 2100 that has much lower uncertainty than the
166   classical Global Circulation Model alternative.
167   An important but subtle EBE - FEBE difference is that whereas the former is an
168   *initial* value problem whose initial condition is the Earth's temperature at $t = 0$, the FEBE
169   is effectively a *past* value problem whose prediction skill improves with the amount of
170   available past data and - depending on the parameters - it can have an enormous memory.
171   To understand this, recall that an important aspect of fractional derivatives is that they are
172   defined as convolutions over various domains. To date, the main one that has been applied
173   to physical problems is the Riemann-Liouville (and the related Caputo) fractional
174   derivative specialized to convolutions over the interval between an initial time = 0 and a
175   later time t. With one or two exceptions, this is the domain considered in Podlubny's
176   mathematical monograph on deterministic fractional differential equations [*Podlubny*,

177   1999] as well as in the stochastic fractional physics discussed in [*West et al.*, 2003],
178   [*Herrmann*, 2011], [*Atanackovic et al.*, 2014], and most of the papers in [*Hilfer*, 2000]
179   (with the partial exceptions of [*Schiessel et al.*, 2000], and [*Nonnenmacher and Metzler*,
180   2000]).   A key point of the FEBE is that it is instead based over semi-infinite domains -
181   here from $-\infty$ to *t* - often called "Weyl" fractional derivatives. This is the natural range to
182   consider for the Earth's energy balance and it is needed to obtain statistically stationary
183   responses. Random walk problems involve fractional equations over the domain 0 to *t* can
184   be dealt with using Laplace transform techniques. In comparison the Earth's temperature
185   balance involves statistically stationary stochastic forcings that are more conveniently dealt
186   with using Fourier techniques.
187   We have mentioned that the FEBE can be derived phenomenologically where the
188   fractional derivative of order *h* term representing the energy storage processes [*Lovejoy et
189   al.*, 2021]. In this approach the order *h* is an empirically determined parameter with *h* = 1
190   corresponding to the classical (exponential) exception. Alternatively it may derived from
191   a more fundamental starting point, the classical heat equation – the same starting point as
192   the classical Budyko-Sellers energy balance models ([*Budyko*, 1969], [*Sellers*, 1969]).
193   Recently it was shown that with the help of Babenko's operator method that the special *h*
194   = 1/2 FEBE - the Half-ordered Energy Balance Equation (HEBE) - could be derived
195   analytically from the classical heat equation [*Lovejoy*, 2021a; b]. To obtain the HEBE, it
196   is sufficient to improve the mathematical treatment of the radiative boundary conditions in
197   the classical energy transport equation: the *h* = 1/2 process discussed below is completely
198   classical (indeed, the use of half order derivatives in heat problems goes back to the 1960's
199   e.g. [*Oldham*, 1973; *Oldham and Spanier*, 1972], [*Babenko*, 1986], [*Magin et al.*, 2004]
200   [*Sierociuk et al.*, 2013]).   The extension to $h \neq 1/2$ can be obtained from the same
201   mathematical techniques by starting with the fractional generalization of the classical heat
202   equation, the fractional heat equation. Further generalizations are also possible and will be
203   reported elsewhere.
204   *The purpose of this paper is to understand various statistical properties of the*
205   *statistically stationary solutions of noise driven fractional relaxation - oscillation*
206   *equations that underpin the FEBE: "fractional Relaxation noise" (fRn) - and its integral*
207   *"fractional Relaxation motion" (fRm) with stationary increments. fRn, fRm are direct*
208   *extensions of the widely studied fractional Gaussian noise (fGn) and fractional Brownian*
209   *motion (fBm) processes, they also generalize the h = 1 Ornstein-Uhlenbeck process. We*
210   *derive the main statistical properties of both fRn and fRm including spectra, correlation*
211   *functions and (stochastic) predictability limits needed for forecasting the Earth*
212   *temperature ([Lovejoy et al., 2015], [Del Rio Amador and Lovejoy, 2019; Del Rio Amador*
213   *and Lovejoy, 2021a; Del Rio Amador and Lovejoy, 2021b]) or projecting it to 2050 or*
214   *2100 [Hébert et al., 2021], [Procyk et al., 2020].*
215   The choice of a Gaussian white noise forcing was made not so much for its theoretical
216   simplicity but for its physical realism. Using scaling to divide atmospheric dynamics into
217   dynamical ranges ([*Lovejoy*, 2013], [*Lovejoy*, 2015a], [*Lovejoy*, 2019b]), the main ones are
218   weather, macroweather and climate. While the temperature variability in both space and
219   in time is generally highly intermittent (multifractal), there is one exception: the temporal
220   macroweather regime (starting at the lifetime of planetary structures - roughly ten days –
221   up until the climate regime at much longer scales). Macroweather is the regime over which
222   the FEBE applies and it has exceptionally low intermittency: temporal (but not spatial)

223 temperature anomalies are not far from Gaussian ([*Lovejoy*, 2018]). Responses to
224 multifractal or Levy process FEBE forcings may however be of interest elsewhere.
225   This paper is structured as follows. In section 2 we present the fractional relaxation
226 equation as a natural generalization of the classical fractional Brownian motion and
227 fractional Gaussian noise processes. When forced by Gaussian white noises, the solutions
228 define the corresponding fractional Relaxation motions (fRm) and fractional Relaxation
229 noises (fRn). We consider the extension when the equation is forced by a scaling noise
230 fGn (this is equivalent to considering the fractionally integrated fractional relaxation
231 equation with white noise forcing). In this section, we first solve the equations in terms
232 of Green's functions, and then introduce powerful Fourier techniques that are needed in
233 section 3 analytically derive the second order statistics including autocorrelations, structure
234 functions, Haar fluctuations and spectra (with many details in appendix A). In section 4
235 we discuss the problem of prediction – important for macroweather forecasting - deriving
236 expressions for the theoretical prediction skill as a function of forecast lead time. In section
237 5 we conclude and in appendix B, we derive the properties of the HEBE special case.

2. The fractional relaxation equation

2.1 fRn, fRm, fGn and fBm

240   In the introduction, we outlined physical arguments that the Earth's global energy
241 balance could be well modelled by the fractional energy balance equation. Taking T as the
242 globally averaged temperature, τ as the characteristic time scale for energy
243 storage/relaxation processes, F as the (stochastic) forcing (energy flux; power per area),
244 and s the climate sensitivity (temperature increase per unit flux of forcing) the FEBE can
245 be written in Langevin form as:

$$\tau^h\left({}_aD_t^hT\right)+T=sF \quad , \tag{1}$$

247 where the Riemann-Liouville fractional derivative symbol ${}_aD_t^h$ is defined as:

$$_aD_t^hT=\frac{1}{\Gamma(1-h)}\frac{d}{dt}\int_a^t(t-s)^{-h}T(s)ds;\quad 0<h<1 \quad , \tag{2}$$

249 Where Γ is the standard gamma function. Derivatives of order $\nu>1$ can be obtained using
250 $\nu = h+m$ where m is the integer part of ν, and then applying this formula to the mth ordinary
251 derivative. The main case studied in applications (e.g. random walks) is $a = 0$ so that
252 Laplace transform techniques are often used (alternatively, the somewhat different Caputo
253 fractional derivative is used). However, here we will be interested in $a=-\infty$: the Weyl
254 fractional derivative $_{-\infty}D_t^h$ which is naturally handled by Fourier techniques (section 2.4
255 and appendices A, B), and in this case, this distinction is unimportant.
256   Since equation 1 is linear, by taking ensemble averages, it can be decomposed into
257 deterministic and random components with the former driven by the mean forcing external
258 to system $<F>$, and the latter by the fluctuating stochastic component $F - <F>$ representing
259 the internal forcing driving the internal variability. The deterministic part has been used to
260 project the Earth's temperature throughout the 21st century ([*Procyk et al.*, 2020]); in the

261 following we consider the simplest purely stochastic model in which $<F> = 0$ and $F = \gamma$
262 where γ is a Gaussian "delta correlated" and unit amplitude white noise:

263
$$\langle \gamma(v) \rangle = 0; \quad \langle \gamma(v) \gamma(u) \rangle = \delta(u-v) \ . \tag{3}$$

264   In [*Hebert*, 2017], [*Lovejoy et al.*, 2017], [*Hébert et al.*, 2021] it was argued on the
265 basis of an empirical study of ocean- atmosphere coupling that $\tau_r \approx 2$ years while recent
266 work indicates a value somewhat higher, ≈ 5 years, [*Procyk et al.*, 2020]. At high
267 frequencies, [*Lovejoy et al.*, 2015] and [*Del Rio Amador and Lovejoy*, 2019], [*Del Rio*
268 *Amador and Lovejoy*, 2021a] that the value $h \approx 0.4$ reproduced both the Earth's temperature
269 both at scales $< \tau$ as well as for macroweather scales (longer than the weather regime
270 scales of about 10 days) but still $< \tau$. [*Procyk et al.*, 2020] also used the FEBE to estimate
271 (the global) $s = [0.45, 0.67]$ K/W/m² (90% confidence interval) and the amplitude of
272 the radiative forcing at monthly resolution was: $[0.89; 1.42]$ W/m² (90% confidence
273 interval).
274   When $0 < h < 1$, eq. 1 with $\gamma(t)$ replaced by a deterministic forcing is a fractional
275 generalization of the usual ($h = 1$) relaxation equation; when $1 < h < 2$, it is the "fractional
276 oscillation equation", a generalization of the usual ($h = 2$) oscillation equation, [*Podlubny*,
277 1999].
278   To simplify the development, we use the relaxation time τ to nondimensionalize time
279 i.e. to replace time by t/τ to obtain the canonical Weyl fractional relaxation equation:

280
$$\left({}_{-\infty}D_t^h + 1 \right) U_h = \gamma; \quad Q_h(t) = \int_0^t U_h(v) dv \tag{4}$$

281 for the nondimensional process U_h. The dimensional solution of eq. 1 with nondimensional
282 $\gamma = sF$ is simply $T(t) = \tau^{-1} U_h(t/\tau)$ so that in the nondimensional eq. 4, the characteristic
283 transition "relaxation" time between dominance by the high frequency (differential) and
284 the low frequency (U_h term) is $t = 1$. Although we give results for the full range $0 < h < 2$
285 - i.e. both the "relaxation" and "oscillation" ranges – for simplicity, we refer to the solution
286 $U_h(t)$ as "fractional Relaxation noise" (fRn) and to $Q_h(t)$ as "fractional Relaxation motion"
287 (fRm). Note that fRn is only strictly a noise when $h \leq 1/2$.
288   In dealing with fRn and fRm, we must be careful of various small and large t
289 divergences. For example, eqs. 1 and 4 are the fractional Langevin equations
290 corresponding to generalizations of integer ordered stochastic diffusion equations: the
291 classical $h = 1$ case is the Ohrenstein-Uhlenbeck process. Since $\gamma(t)$ is a "generalized
292 function" - a "noise" - it does not converge at a mathematical instant in time, it is only
293 strictly meaningful under an integral sign. Therefore, a standard form of eq. 4 is obtained
294 by integrating both sides by order h (i.e. by differentiating by $-h$ and assuming that
295 differentiation and integration of order h commute):

296
$$U_h(t) = -{}_{-\infty}D_t^{-h}U_h + {}_{-\infty}D_t^{-h}\gamma = -\frac{1}{\Gamma(h)}\int_{-\infty}^t (t-v)^{h-1} U_h(v) dv + \frac{1}{\Gamma(h)}\int_{-\infty}^t (t-v)^{h-1} \gamma(v) dv,$$

297
$$\tag{5}$$

298 (see e.g. [*Karczewska and Lizama*, 2009]). The white noise forcing in the above is
299 statistically stationary; the solution for $U_h(t)$ is also statistically stationary. It is tempting
300 to obtain an equation for the motion $Q_h(t)$ by integrating eq. 4 from $-\infty$ to t to obtain the

301 fractional Langevin equation: $_{-\infty}D_t^h Q_h + Q_h = W$ where W is Wiener process (a standard

302 Brownian motion) satisfying $dW = \gamma(t)dt$. Unfortunately the Wiener process integrated

303 $-\infty$ to t almost surely diverges, hence we relate Q_h to U_h by an integral from 0 to t.

304   In the high frequency limit, the derivative dominates and we obtain the simpler

305 fractional Langevin equation:

306
$$_{-\infty}D_t^h F_h = \gamma; \qquad B_h(t) = \int_0^t F_h(v)dv \qquad (6)$$

307 Whose solution F_h is the fractional Gaussian noise process (fGn, not to be confused with

308 the forcing), and whose integral B_h is fractional Brownian motion (fBm). We thus

309 anticipate that F_h and B_h are the high frequency limits of fRn, fRm.

2.2 Green's functions

311   Although it will turn out that Fourier techniques are very convenient for calculating

312 the statistics, there are also advantages to classical (real space) approaches and in any case

313 they are needed for studying the predictability properties (section 4). We therefore start

314 with a discussion of Green's functions that are the classical tools for solving

315 inhomogeneous linear differential equations:

316
$$F_h(t) = \int_{-\infty}^t G_{0,h}^{(fGn)}(t-v)\gamma(v)dv$$
$$U_h(t) = \int_{-\infty}^t G_{0,h}^{(fRn)}(t-v)\gamma(v)dv \qquad , \qquad (7)$$

317 where $G_{0,h}^{(fGn)}$ and $G_{0,h}^{(fRn)}$ are Green's functions for the differential operators corresponding

318 respectively to $_{-\infty}D_t^h$ and $_{-\infty}D_t^h + 1$. Note that due to causality, all the Green's functions

319 used in this paper vanish for $t < 0$.

320    $G_{0,h}^{(fGn)}$ and $G_{0,h}^{(fRn)}$ are the usual "impulse" (Dirac) response Green's functions (hence

321 the subscript "0"). For the differential operator Ξ they satisfy:

322
$$\Xi G_{0,h}(t) = \delta(t). \qquad (8)$$

323   Integrating this equation we find an equation for their integrals $G_{1,h}$ which are thus

324 "step" (Heaviside, subscript "1") response Green's functions satisfying:

325
$$\Xi G_{1,h}(t) = \Theta(t); \quad \Theta(t) = \int_{-\infty}^t \delta(v)dv \; ; \qquad \frac{dG_{1,h}}{dt} = G_{0,h}, \qquad (9)$$

326 where Θ is the Heaviside (step) function (= 0 for $t < 0$, = 1 for $t \geq 0$). The inhomogeneous

327 equation:

328
$$\Xi f(t) = F(t) \qquad (10)$$

329 has a solution in terms of either an impulse or a step Green's function:

330
$$f(t)=\int_{-\infty}^{t}G_{0,h}(t-v)F(v)dv=\int_{-\infty}^{t}G_{1,h}(t-v)F'(v)dv; \quad F'(v)=\frac{dF}{dv} \quad , \tag{11}$$

331 the equivalence being established by integration by parts with the conditions $F(-\infty)=0$
332 and $G_{1,h}(0)=0$. The use of the step rather than impulse response is standard in the Energy
333 Balance Equation literature since it gives direct information on energy balance and the
334 approach to equilibrium (see e.g. [*Lovejoy et al.*, 2021]). The step response for the noise
335 is also the basic impulse response function for the motion.
336   For fGn, the Green's functions are simply the kernels of the fractional integrals:

337
$$F_{h}(t)=\frac{1}{\Gamma(h)}\int_{-\infty}^{t}(t-v)^{h-1}\gamma(v)dv, \tag{12}$$

338 obtained by integrating both sides of eq. 6 by order h. We conclude:

339
$$G_{0,h}^{(fGn)}=\frac{t^{h-1}}{\Gamma(h)}; \quad G_{1,h}^{(fGn)}=\frac{t^{h}}{\Gamma(h+1)}; \quad -\frac{1}{2}\leq h<\frac{1}{2} \quad . \tag{13}$$

340   For fRn, we now recall some classical results useful in geophysical applications.
341 First, these Green's functions are often equivalently written in terms of Mittag-Leffler
342 functions ("generalized exponentials"), $E_{\alpha,\beta}$:

343
$$G_{0,h}(t)=t^{h-1}E_{h,h}(-t^{h}); \quad E_{\alpha,\beta}(z)=\sum_{n=0}^{\infty}\frac{z^{n}}{\Gamma(\alpha n+\beta)} \tag{14}$$

344
$$G_{0,h}(t)=\sum_{n=1}^{\infty}(-1)^{n+1}\frac{t^{nh-1}}{\Gamma(nh)}; \quad 0<h\leq 2$$

345 (to lighten the notation in eq. 14 and in the following, we suppress the superscripts for fRn,
346 fRm proceesses). A convenient feature of Mittag-Leffler functions is that they can be
347 easily integrated by any positive order α:

348
$$G_{\alpha,h}(t)={}_{0}D_{t}^{-\alpha}(G_{0,h}(t))=\begin{array}{ll}t^{h-1+\alpha}E_{h,h+\alpha}(-t^{h})=t^{\alpha-1}\sum_{n=1}^{\infty}(-1)^{n+1}\frac{t^{nh}}{\Gamma(\alpha+nh)}; & t\geq 0\\ 0; & t<0\end{array}$$

349
$$\alpha\geq 0; \quad 0\leq h\leq 2 \tag{15}$$

350 ([*Podlubny*, 1999]). We have added the constraint $t>0$ since due to causality, physical
351 Green's functions vanish for negative arguments. In the following this will simply be
352 assumed. With $\alpha=1$, we obtain the useful formula:

353
$$G_{1,h}(t)=t^{h}E_{h,h+1}(-t^{h}); \quad G_{1,h}(t)=\sum_{n=1}^{\infty}(-1)^{n+1}\frac{t^{nh}}{\Gamma(1+nh)} \tag{16}$$

354   With this, we see that $G_{0,h}^{(fGn)}$ and $G_{1,h}^{(fGn)}$ are simply the first terms in the power series

355   expansions of the corresponding fRn, fRm Green's functions. The solution to eq. 4 with

356   the white noise forcing $\gamma(t)$ is therefore:

357
$$U_{0,h}(t) = \int_{-\infty}^{t} G_{0,h}(t-v)\gamma(v)dv \qquad (17)$$

358   Where for this "pure" fRn process, we have added the subscript "0" for reasons

359   discussed below. We note that at the origin, for $0 < h < 1$, $G_{0,h}$ is singular whereas $G_{1,h}$ is

360   regular so that it is may be advantageous to use the latter (step) response function (for

361   example in the numerical simulations in section 4). These Green's function responses are

362   shown in figure 1. When $0 < h \leq 1$, the step response is monotonic; in an energy balance

363   model, this would correspond to relaxation to equilibrium. When $1 < h < 2$, we see that

364   there is overshoot and oscillations around the long term value; it is therefore (presumably)

365   outside the physical range of an equilibrium process.

366   In order to understand the relaxation process – i.e. the approach to the asymptotic

367   value 1 in fig. 1 for the step response $G_{1,h}$ - we need the asymptotic expansion:

368
$$G_{\alpha,h}(t) = \sum_{n=0}^{\infty} \frac{(-1)^n}{\Gamma(\alpha - nh)} t^{\alpha-1-nh}; \quad t \gg 1 \quad , \qquad (18)$$

369   For $\alpha = 0, 1$ we obtain the special cases corresponding to impulse and step responses:

370
$$G_{0,h}(t) = \sum_{n=0}^{\infty} (-1)^n \frac{t^{-1-nh}}{\Gamma(-nh)}; \quad G_{1,h}(t) = \sum_{n=0}^{\infty} (-1)^n \frac{t^{-nh}}{\Gamma(1-nh)}; \quad t \gg 1 \qquad (19)$$

371   ($0 < h < 1$, $1 < h < 2$; note that the $n = 0$ terms are 0, 1 for $G_{0,h}$, $G_{1,h}$ respectively) [*Podlubny*,

372   1999], i.e. the asymptotic expansions are power laws in t^{-h} rather than t^h. According to this,

373   the asymptotic approach to the step function response (bottom row in fig. 1) is a slow,

374   power law process. In the FEBE, this implies for example that the classical CO_2 doubling

375   experiment would yield a power law rather than exponential approach to a new

376   thermodynamic equilibrium. Comparing this to the EBE, i.e. the special case $h = 1$, we

377   have:

378
$$G_{0,1}(t) = e^{-t}; \quad G_{1,1}(t) = 1 - e^{-t} \quad , \qquad (20)$$

379   so that when $h = 1$, the asymptotic step response is instead approached exponentially fast.

380   We see that when $h = 1$ the process is a classical Ornstein-Uhlenbeck process so that fRn

381   can be considered a generalization of the latter. There are also analytic formulae for fRn

382   when $h = 1/2$ (the HEBE) discussed in appendix B notably involving logarithmic

383   corrections.

384

Commented [SL1]: Corrected sign! -1**n not -1**(n+1)
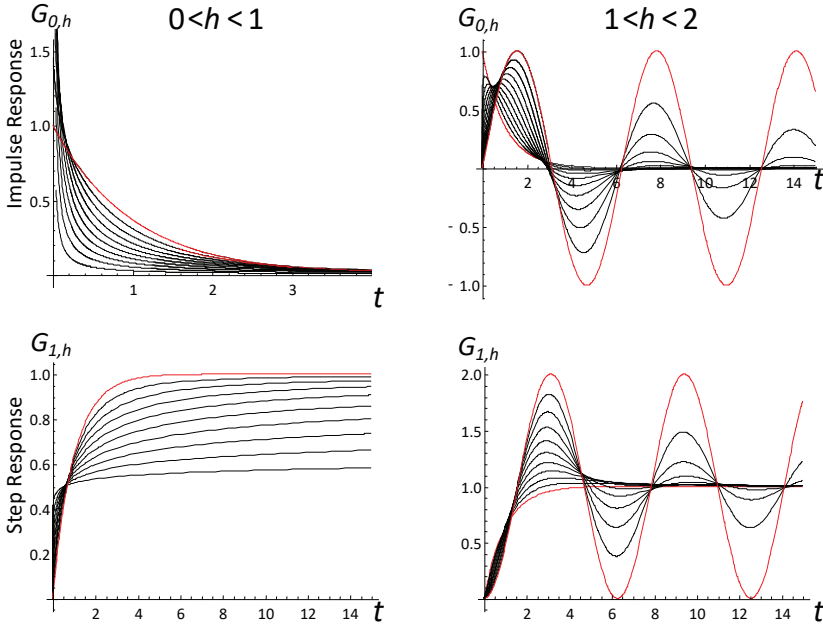
Fig. 1a: The impulse (top) and step response functions (bottom) for the fractional relaxation range ($0 < h < 1$, left, red is $h = 1$, the exponential), the black curves, bottom to top are for $h = 1/10$, $2/10$, ..$9/10$) and the fractional oscillation range ($1 < h < 2$, red are the integer values $h = 1$, bottom, the exponential, and top, $h = 2$, the sine function, the black curves, bottom to top are for $h = 11/10$, $12/10$, ..$19/10$.

2.3 The α order fractionally integrated fRn, fRm processes:

Before proceeding to discuss the statistics of fRn, fRm processes, it is useful to make a generalization to the fractionally integrated processes:

$$U_{\alpha,h} = {}_{-\infty}D_t^{-\alpha}U_{0,h} \tag{21}$$

$U_{\alpha,h}$ is the "α order integrated, fractional h relaxation noise". Combined with the Green's function relation $G_{\alpha,h} = {}_{-\infty}D_t^{-\alpha}G_{0,h}$ (eq. 15; recall that $G_{0,h}(t) = 0$ for $t<0$), we find that $U_{\alpha,h}$, $G_{\alpha,h}$ are respectively the fractionally integrated relaxation noises and Green's functions of the fractionally integrated fractional relaxation equation:

$$\left({}_{-\infty}D_t^{\alpha+h} + {}_{-\infty}D_t^{\alpha}\right)U_{\alpha,h} = \gamma; \quad \left({}_{-\infty}D_t^{\alpha+h} + {}_{-\infty}D_t^{\alpha}\right)G_{\alpha,h} = \delta(t) \tag{22}$$

If the highest order derivative is constrained to be an integer (i.e. $\alpha+h = 1$ or 2), then the equation is a standard fractional Langevin equation, for example U could for the velocity of a particle with fractional damping and white noise forcing, although even here, the initial conditions are usually taken to be at $t = 0$ not $t = -\infty$. Equivalently, $U_{\alpha,h}$, is the solution of the relaxation equation but with an fGn forcing:

$$\left(_{-\infty}D_t^h + 1\right)U_{\alpha,h} = {_{-\infty}}D_t^{-\alpha}\gamma = F_\alpha(t); \quad 0 \le \alpha < 1/2 \tag{23}$$

(the Weyl fractional derivatives commute). F_α is the α order fGn process, and the restriction $\alpha < 1/2$ is needed to ensure low frequency convergence (see below).

In the Earth's radiative balance, such fractionally integrated fRn processes arise in two physically interesting situations. The first is where the forcing itself has a long memory – e.g. it is an fGn process. Whereas the memory in a pure fRn process is purely from the high frequency storage term, in this case, the forcing (the overall radiative imbalance) also contributes to the memory and this has important consequences for the predictability (section 4). Although the solutions $U_{\alpha,h}$ are mathematically the same whether from the fractional relaxation equation with fGn forcing (eq. 23) or the fractionally integrated fractional relaxation equation with white noise forcing (eq. 22), only the former is directly relevant for the Earth energy balance. This is because the energy balance involves the response from both stochastic (internal) *and* deterministic (external) forcing. For the latter, it is important that following a step function forcing, at long times, the system will approach a new state of thermodynamic equilibrium. This implies that the term in the equation that dominates at low frequencies – the lowest order term - be of order zero so that if F in eq. 1 is a step function, that the new equilibrium temperature (anomaly) is $T = sF$.

The second situation where fractionally integrated fRn processes arise is for the energy storage (even in the purely white noise forcing case). The storage process is the difference between the forcing and the response:

$$S_{\alpha,h} = F_\alpha - U_{\alpha,h} \tag{24}$$

so that:

$$S_{\alpha,h} = {_{-\infty}}D_t^h U_{\alpha,h} = U_{h-\alpha,h} \tag{25}$$

Even when the forcing is pure white noise ($\alpha = 0$), the storage is an h ordered fractionally integrated process: $S_{0,h} = U_{h,h}$; this corresponds to the storage following an impulse forcing.

The storage following a step forcing is obtained by integration order 1: $U_{1+h,h}$. Similarly, the Green's function for the fRn storage following an impulse forcing is $G_{h,h}$ and following a step forcing, $G_{1+h,h}$ (fig. 1b). Since it turns out that most of the pure fRn ($\alpha = 0$) results are readily generalized to $0<\alpha<1/2$, many fractionally integrated results are given below.
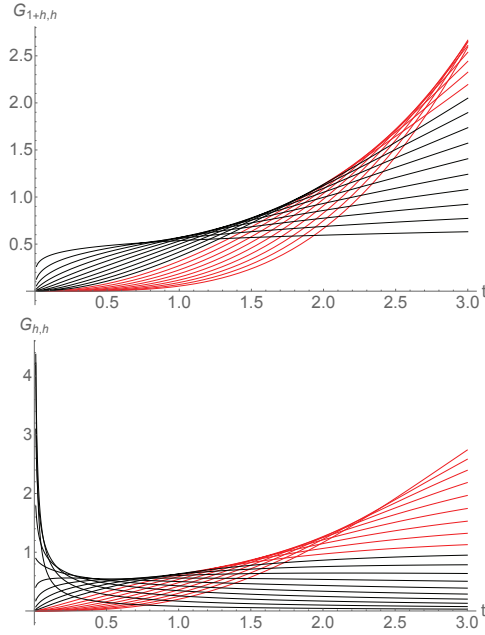
Fig. 1b: The storage Green's functions for the fractional relaxation equation ($\alpha = 0$): top impulse response ($G_{h,h}$), bottom, step response ($G_{1+h,h}$). Black is for $h = 1/10, 2/10,..10/10$, red for $11/10, 12/10, …19/10$ (to identify the curves, use the fact that at large t, they are in order of increasing h (bottom to top). For small t, $G_{h,h} \propto t^{2h-1}$ (eq. 15) so that for $h \leq 1/2$, the impulse response is singular at the origin. For large t, $G_{h,h} \propto t^{h-1}$ (eq. 18) so that for $h<1$, the total impulse response storage decreases following the impulse, for $h = 1$ (the EBE), it tends to unity and for $h>1$, it diverges.

2.4 Statistics

In the above, we discussed fGn, fRn and their order one integrals fBm, fRm as well as fractional generalizations, presenting a classical (real space) approach stressing the links with fGn, fBm, we now turn to their statistics. $U_{\alpha,h}(t)$ is a mean zero stationary Gaussian process (i.e. $<U_{\alpha,h}(t)> = 0$ where "<.>" indicates ensemble or statistical averaging), therefore its statistics are determined completely by it's autocorrelation function $R_{\alpha,h}(t)$ which is only a function of the lag t:

$$R_{\alpha,h}(t) = \left\langle U_{\alpha,h}(t+v)U_{\alpha,h}(v) \right\rangle = \int_0^\infty G_{\alpha,h}(t+v)G_{\alpha,h}(v)\,dv \qquad (26)$$

452 The far right equality follows from $U_{\alpha,h} = G_{\alpha,h} * \gamma$ and $\langle \gamma(t)\gamma(t') \rangle = \delta(t-t')$ ("*"

453 indicates "convolution"). The process can only be normalized by $R_{\alpha,h}(0)$ when there is

454 no small scale divergence i.e. when:

455
$$R_{\alpha,h}(0) = \langle U_{\alpha,h}^2 \rangle = \int_0^\infty G_{\alpha,h}(v)^2 \, dv < \infty; \quad \alpha + h > 1/2 \tag{27}$$

456 When $\alpha+h<1/2$, this diverges in order to be normalized, the process must be averaged at a
457 finite resolution (below).

458 Although it is possible to follow [*Mandelbrot and Van Ness*, 1968] and derive many
459 statistical properties in real space, a Fourier approach is not only more streamlined, but is
460 more powerful. The reason for the simplicity of the Fourier approach is that the Fourier
461 Transform (*FT*, indicated by the tilda) of the Weyl fractional derivative is symbolically:

462
$$(i\omega)^h \overset{FT}{\leftrightarrow} {}_{-\infty}D_t^h \tag{28}$$

463 (e.g. [*Podlubny*, 1999], this is simply the extension of the usual rule for the *FT* of integer-
464 ordered derivatives). Therefore since $U_{\alpha,h}$, $G_{\alpha,h}$ are respectively solutions and Green's
465 functions of the fractionally integrated fractional relaxation equation (eq. 22) we have:

466
$$\left((i\omega)^{\alpha+h} + (i\omega)^\alpha\right)\tilde{U}_{\alpha,h} = \tilde{\gamma} \overset{FT}{\leftrightarrow} \left({}_{-\infty}D_t^{\alpha+h} + {}_{-\infty}D_t^\alpha\right)U_{\alpha,h} = \gamma, \tag{29}$$

467
$$\left((i\omega)^{\alpha+h} + (i\omega)^\alpha\right)\tilde{G}_{\alpha,h} = 1 \overset{FT}{\leftrightarrow} \left({}_{-\infty}D_t^{\alpha+h} + {}_{-\infty}D_t^\alpha\right)G_{\alpha,h} = \delta$$

468 So that:

469
$$\tilde{U}_{\alpha,h}(\omega) = \frac{\tilde{\gamma}}{(i\omega)^\alpha\left(1+(i\omega)^h\right)}; \quad \tilde{G}_{\alpha,h}(\omega) = \frac{1}{(i\omega)^\alpha\left(1+(i\omega)^h\right)}; \quad 0<\alpha<1; \quad 0<h<2$$

470
$$\tag{30}$$

471 We see that in the limit $h\to 0$, $U_{\alpha,0}$ is an α order fGn process (see e.g. eq. 23).

472 Now we can use the fact that the white noise γ has a flat spectrum:

473
$$\langle \tilde{\gamma}(\omega)\tilde{\gamma}(\omega') \rangle = \delta(\omega+\omega')\left\langle \left|\tilde{\gamma}(\omega)\right|^2 \right\rangle = 2\pi\delta(\omega+\omega') \overset{FT}{\leftrightarrow} \langle \gamma(t)\gamma(t') \rangle = \delta(t-t')$$

474
$$\tag{31}$$

475 The modulus (vertical bars) intervene since for any real function $f(t)$ we have

476 $\tilde{f}(\omega) = \tilde{f}^*(-\omega)$, where the superscript "*" indicates complex conjugate.

477 Application of eq. 31 leads to:

478
$$R_{\alpha,h}(t) = \frac{1}{2\pi}\int_{-\infty}^\infty e^{i\omega t} E_U(\omega) \, d\omega; \quad E_U(\omega) = \left\langle \left|\tilde{U}_{\alpha,h}(\omega)\right|^2 \right\rangle = \frac{1}{|\omega|^{2\alpha}\left(1+(-i\omega)^h\right)\left(1+(i\omega)^h\right)}$$

479
$$\tag{32}$$

480 i.e. the spectrum E_U is the *FT* of the correlation function $R_{\alpha,h}(t)$ (the Wiener-Khintchin
481 theorem). Applying this to $U_{\alpha,h}$, we obtain:

$$R_{\alpha,h}(t) = \frac{1}{2\pi} \int_{-\infty}^{\infty} \frac{\cos(\omega t)\,d\omega}{|\omega|^{2\alpha}\left(1+(i\omega)^h\right)\left(1+(-i\omega)^h\right)} \qquad (33)$$

483 This shows that $R_{\alpha,h}(t) = R_{\alpha,h}(-t)$ so that below, we only consider $t\geq0$.

484 Since, $R_{\alpha,h}(0)$ diverges for $\alpha+h<1/2$, we consider the integral $Q_{\alpha,h}$ of the process
485 (the "motion") from which we can easily compute the average. The corresponding variance
486 $V_{\alpha,h}$ is:

$$V_{\alpha,h}(t) = \left\langle Q_{\alpha,h}(t)^2 \right\rangle; \quad Q_{\alpha,h}(t) = \int_0^t U_{\alpha,h}(v)\,dv \qquad (34)$$

488 In terms of $\widetilde{U}_{\alpha,h}(\omega)$:

$$V_{\alpha,h}(t) = \frac{1}{\pi}\int_{-\infty}^{\infty}\frac{(1-\cos\omega t)}{\omega^2}\left\langle\left|\widetilde{U}_{\alpha,h}(\omega)\right|^2\right\rangle d\omega = \frac{1}{\pi}\int_{-\infty}^{\infty}\frac{(1-\cos\omega t)}{|\omega|^{2+2\alpha}}\frac{d\omega}{\left(1+(i\omega)^h\right)\left(1+(-i\omega)^h\right)}$$

490 $$\alpha<1/2, \qquad 0<h<2. \quad (35)$$
491 We see that at low frequencies, when $\alpha\geq1/2$ the integral diverges for all t. Also note that
492 a series expansion for $V_{\alpha,h}(t)$ in t will have only even ordered integer power terms.
493 Comparing eqs. 33, 35 we see that $R,\ V$ are linked by the simple relation:

$$R_{\alpha,h}(t) = \frac{1}{2}\frac{d^2 V_{\alpha,h}(t)}{dt^2} \qquad (36)$$

495 Therefore by integrating eq. 26 (twice), we can express $V_{\alpha,h}$ in terms of $G_{\alpha,h}$:

$$V_{\alpha,h}(t) = \int_0^{\infty}\left(G_{\alpha+1,h}(t+v) - G_{\alpha+1,h}(v)\right)^2 dv + \int_0^t G_{\alpha+1,h}(v)^2\,dv \qquad (37)$$

497 This can be verified by differentiation and using $\dfrac{dG_{\alpha+1,h}}{dt} = G_{\alpha,h}$.

498 The basic behaviour can be understood in the Fourier domain. First, putting $t = 0$ in
499 eq. 32 (i.e. "Parseval's theorem") we have:

$$R_{\alpha,h}(0) = \frac{1}{2\pi}\int_{-\infty}^{\infty}E_U(\omega)\,d\omega = \frac{1}{2\pi}\int_{-\infty}^{\infty}\frac{d\omega}{|\omega|^{2\alpha}\left(1+(i\omega)^h\right)\left(1+(-i\omega)^h\right)} \qquad (38)$$

501 So that when $\alpha+h<1/2$, R diverges at high frequencies (small t), hence to represent a
502 physical process (here, the Earth's temperature), the process must be averaged over a finite
503 resolution τ. When $\alpha+h>1/2$, $R(0)$ is finite and can therefore be used to obtain a normalized
504 autocorrelation function (eq. 27).
505 From eq. 32, we may also easily obtain the asymptotic high and low frequency
506 behaviours of the energy spectrum:

507
$$E_U(\omega) \propto \begin{array}{ll} \omega^{-2(\alpha+h)} + O(\omega^{-2\alpha-3h}); & \omega \gg 1 \\ \omega^{-2\alpha} - 2\cos\left(\dfrac{\pi h}{2}\right)\omega^{h-2\alpha} + O(\omega^{2h-2\alpha}) & \omega \ll 1 \end{array} \qquad (39)$$

2.5 Finite resolution processes

508
509 When $\alpha+h<1/2$ the process doesn't converge at any instant t, it is a noise, a
510 generalized function. To represent the Earth's temperature it must therefore be averaged
511 at a finite resolution τ:

512
$$U_{\alpha,h,\tau}(t) = \frac{Q_{\alpha,h}(t) - Q_{\alpha,h}(t-\tau)}{\tau}. \qquad (40)$$

513 Applying eq. 34, 40, we obtain the "resolution τ" autocorrelation:

514
$$R_{\alpha,h,\tau}(\Delta t) = \langle U_{\alpha,h,\tau}(t)U_{\alpha,h,\tau}(t-\Delta t)\rangle = \tau^{-2}\langle(Q_{\alpha,h}(t)-Q_{\alpha,h}(t-\tau))(Q_{\alpha,h}(t-\Delta t)-Q_{\alpha,h}(t-\Delta t-\tau))\rangle$$
$$= \tau^{-2}\frac{1}{2}(V_{\alpha,h}(\Delta t-\tau)+V_{\alpha,h}(\Delta t+\tau)-2V_{\alpha,h}(\Delta t)) \qquad \Delta t \geq \tau$$

515
$$R_{\alpha,h,\tau}(0) = \tau^{-2}V_{\alpha,h}(\tau), \qquad (41)$$

516 Alternatively, measuring time in units of the resolution $\lambda = \Delta t/\tau$:

517
$$R_{\alpha,h,\tau}(\lambda\tau) = \langle U_{\alpha,h,\tau}(t)U_{\alpha,h,\tau}(t-\lambda\tau)\rangle = \tau^{-2}\frac{1}{2}(V_{\alpha,h}((\lambda-1)\tau)+V_{\alpha,h}((\lambda+1)\tau)-2V_{\alpha,h}(\lambda\tau)); \quad \lambda \geq 1$$

518
$$(42)$$

519 $R_{a,h,\tau}$ can be conveniently written in terms of centred finite differences:

520
$$R_{\alpha,h,\tau}(\lambda\tau) = \frac{1}{2}\Delta_\tau^2 V_{\alpha,h}(\lambda\tau) \approx \frac{1}{2}V_{\alpha,h}''(\Delta t); \quad \Delta_\tau f(t) = \frac{f(t+\tau/2)-f(t-\tau/2)}{\tau}.$$

521
$$(43)$$

522 The finite difference formula is valid for $\Delta t \geq \tau$. For finite τ, it allows us to obtain the
523 correlation behaviour by replacing the second difference by a second derivative, an
524 approximation that is very good except when Δt is close to τ. Taking the limit $\tau \to 0$ in
525 eq. 43 we obtain the second derivative formula eq. 36.

3 Application to fBm, fGn, fRm, fRn

526

3.1 fBm, fGn

527

528 The above derivations were for noises and motions derived from differential
529 operators whose impulse and step Green's functions had convergent $V_{\alpha,h}(t)$. Before
530 applying them to fRn, fRm, we illustrate this by applying them first to fBm and fGn.
531 The fBm results are obtained by using the fGn step Green's function (eq. 13) in eq.
532 35 with $h = 0$ to obtain:

533
$$V_h^{(fBm)}(t) = 4V_{\alpha=h,0}(t) = \left(\frac{2\sin(\pi h)\Gamma(-1-2h)}{\pi} \right) t^{2h+1}; \quad -\frac{1}{2} \le h < \frac{1}{2} \; .$$

534
(44)

> **Commented [SL2]:** Note the -ve sign removed!

535   The standard normalization and parametrisation is:

$$N_h = K_h = \left(\frac{\pi}{2\sin(\pi h)\Gamma(-1-2h)} \right)^{1/2}$$
$$\qquad = \left(-\frac{\pi}{2\cos(\pi H)\Gamma(-2H)} \right)^{1/2} ; \qquad H = h + \frac{1}{2}; \quad 0 \le H < 1$$

536
(45)

> **Commented [SL3]:** Changed sign and removed bad numerator factor

537   This normalization turns out to be convenient not only for fBm but also for fRm so that for
538   the normalized process:

539
$$V_H^{(fBm)}(t) = t^{2h+1} = t^{2H}; \quad 0 \le H < 1 \; ,$$
(46)

540   Where we have introduced the standard fBm parameter $H = h+1/2$ so that:

541
$$\left\langle \Delta B_H(\Delta t)^2 \right\rangle^{1/2} = \Delta t^H; \quad \Delta B_H(\Delta t) = B_H(t) - B_H(t - \Delta t) \; ,$$
(47)

542   hence H is the fluctuation exponent for fBm. Note that fBm is usually *defined* as the
543   Gaussian process with V_H given by eq. 46 i.e. with this normalization (e.g. [*Biagini et al.,*
544   *2008*]).
545   We can now calculate the correlation function relevant for the fGn statistics. With
546   the above normalization:

$$R_{h,\tau}^{(fGn)}(\lambda\tau) = \frac{1}{2}\tau^{2h-1}\left((\lambda+1)^{2h+1} + (\lambda-1)^{2h+1} - 2\lambda^{2h+1} \right); \quad \lambda \ge 1; \quad -\frac{1}{2} < h < \frac{1}{2}$$

$$R_{h,\tau}^{(fGn)}(0) = \tau^{2h-1}$$

547

548
$$R_{H,\tau}^{(fGn)}(\lambda\tau) \approx h(2h+1)(\lambda\tau)^{2h-1} = H(2H-1)(\lambda\tau)^{2(H-1)}; \quad \lambda \gg 1 \; , \quad (48)$$

549   the bottom approximations are valid for large scale ratios λ. We note the difference in sign
550   for $H > \frac{1}{2}$ ("persistence"), and for $H < \frac{1}{2}$ ("antipersistence"). When $H = \frac{1}{2}$, the noise
551   corresponds to standard Brownian motion, it is uncorrelated.

552   **3.2 fRm, fRn**

553   3.2.1 $R_{\alpha,h}(t)$
554   Since fRm, fRn are Gaussian, their properties are determined by their second order
555   statistics, by $V_{\alpha,h}(t)$, $R_{\alpha,h}(t)$. These statistics are second order in $G_{\alpha,h}(t)$ and can most easily
556   be determined using the Fourier representation of $G_{\alpha,h}(t)$, (section 2.4, appendix A, B). The
557   development is challenging because unlike the $G_{\alpha,h}(t)$ functions that are entirely expressed
558   in series of fractional powers of t, $V_{\alpha,h}(t)$ and $R_{\alpha,h}(t)$ involve mixed fractional and integer

power expansions, the details are given in the appendices, here we summarize the main results.

First, for the noises, we have:

$$R_{\alpha,h}(t) = \sum_{n=2}^{\infty} D_n \Gamma(1 - hn - 2\alpha) t^{-1+hn+2\alpha} + \sum_{j=1,odd}^{\infty} F_j \frac{t^{j-1}}{\Gamma(j)};$$

$$F_j = -\frac{\cos\pi\left(\frac{h}{2}+\alpha\right)}{h\sin\left(\frac{\pi h}{2}\right)\sin\left(\frac{\pi}{h}(j-2\alpha)\right)}; \qquad D_n = (-1)^n \frac{\sin\left(\frac{n\pi h}{2}+\alpha\pi\right)\sin\left(\frac{(n-1)\pi h}{2}\right)}{\pi\sin\left(\frac{\pi h}{2}\right)}$$

$$(49)$$

At small t, the lowest order terms dominate, the normalized autocorrelations are thus:

$$R_{\alpha,h}^{(norm)}(t) = (h+\alpha)(1+2(h+\alpha))t^{-1+2(h+\alpha)} + O(t^{-1+3h+2\alpha}); \qquad \tau \ll t \ll 1; \quad 0 < (h+\alpha) < 1/2$$

$$R_{\alpha,h}^{(norm)}(t) = 1 - \frac{\left|\Gamma(1-2(h+\alpha))\right|\sin(\pi(h+2\alpha))}{\pi F_1} t^{-1+2(h+\alpha)} + O(t^{-1+3h+2\alpha}); \qquad \begin{array}{c} t \ll 1; \\ 1/2 < (h+\alpha) < 3/2 \end{array}$$

$$R_{\alpha,h}^{(norm)}(t) = 1 + \frac{t^2}{2F_1}F_3 + O(t^{-1+2(h+\alpha)})...; \qquad t \ll 1; \quad 3/2 < (h+\alpha) < 2$$

$$(50)$$

(note $F_3 < 0$ for $3/2 < h+\alpha < 2$, see appendix A). We see that at small t, the behaviour of the normalized autocorrelations depend essentially on the sum $h+\alpha$, in particular, when $h+\alpha < 1/2$, the process is effectively an fGn process with effective fluctuation exponent $H = -\frac{1}{2} + (h+\alpha)$. This is to be expected since $\alpha+h$ is the highest order term in the fractionally integrated fractional relaxation equation (eq. 22).

3.2.2 $V_{\alpha,h}(t)$

Integrating twice $V_{\alpha,h}(t) = 2\int_0^t\left(\int_0^v R_{\alpha,h}(u)du\right)dv$, we obtain:

$$V_{\alpha,h}(t) = 2\sum_{n=2}^{\infty} D_n \Gamma(-1-hn-2\alpha)t^{1+hn+2\alpha} + 2\sum_{j=1,odd}^{\infty} F_j \frac{t^{j+1}}{\Gamma(j+2)}; \qquad 0 < h < 2; \quad 0 \le \alpha < 1/2$$

$$(51)$$

When $0 < \alpha+h < 1/2$, the leading ($n = 2$) term for $V_{\alpha,h}$ is $t^{1+2(h+\alpha)}$, ($\propto V_{\alpha+h}^{(fBm)}$) so that the fBm coefficient can be used for normalization using $R_{\alpha,h,\tau}(0) = \tau^{-2}V_{\alpha,h}(\tau)$. When $h+\alpha > 1/2$, this normalization becomes negative, so that it cannot be used, however in this case, $R_{\alpha,h}(0) = F_1$ and may be used for normalization instead. For an analytic expression, convergence

584 properties including numerical results and modified expansions that converge more rapidly,
585 see appendix A, for the special case $h = 1/2$, appendix B.
586   For convenience, the leading terms of the normalized $V_{\alpha,h}$ are:

587
$$V_{\alpha,h}^{(norm)}(t) = t^{1+2(h+\alpha)} + O\left(t^{1+3h+2\alpha}\right) + O\left(t^2\right); \quad 0 < (h+\alpha) < 1/2 \tag{52}$$

588
$$V_{\alpha,h}^{(norm)}(t) = t^2 - \frac{2\Gamma\left(-1-2(h+\alpha)\right)\sin\left(\pi(h+2\alpha)\right)}{\pi F_1} t^{1+2(h+\alpha)} + O\left(t^{1+3h+2\alpha}\right); \quad 1/2 < (h+\alpha) < 3/2$$

589
$$V_{\alpha,h}^{(norm)}(t) = t^2 + \frac{F_3}{12 F_1} t^4 + O\left(t^{2(h+\alpha)+1}\right); \quad 3/2 < (h+\alpha) < 2$$

590

591 ### 3.2.3 Asymptotic expansions
592   For multidecadal global climate projections, the relaxation time has been estimated
593 at ≈ 5 years ([*Procyk et al.*, 2020]), so that we are interested in the long time behaviour
594 (exploited for example in [*Hébert et al.*, 2021]). For this, asymptotic expansions are needed,
595 in appendix A we show:

596
$$R_{\alpha,h}(t) = -\sum_{n=0}^{\infty} D_{-n} \Gamma\left(1 + nh - 2\alpha\right) t^{2\alpha-(1+nh)} + P_{\alpha,h,+}(t); \quad t \gg 1 \tag{53}$$

597 Where the $P_{\alpha,h,+}(t) = 0$ for $h<1$ while for $1<h<2$ it has exponentially damped oscillations
598 (see fig. 2 lower right and appendix A).
599   For pure fRn processes a useful formula is:

600
$$R_{0,h}(t) = \sum_{n=1}^{\infty} (-1)^n \frac{1 + \cot\left(\frac{\pi h}{2}\right)\tan\left(\frac{n\pi h}{2}\right)}{2\Gamma(-nh)} t^{-(1+nh)} + P_{0,h,+}(t); \qquad\qquad t \gg 1$$

601 (54)
602 Or more generally:

603
$$R_{\alpha,h}(t) = \frac{\Gamma(1-2\alpha)\sin(\pi\alpha)}{\pi} t^{2\alpha-1} - \frac{\cos\left(\frac{\pi h}{2}\right)}{\cos\left(\frac{\pi h}{2} - \pi\alpha\right)\Gamma(2\alpha - h)} t^{2\alpha-(1+h)} + \dots$$

604            $t \gg 1;$ $0 \leq h < 2;$ $0 \leq \alpha < 1/2$ (55)
605 We see that when $\alpha \neq 0$, $D_0 > 0$ so that as expected, the leading behaviour has no h
606 dependence, it is only due to the long range correlations in the forcing; we obtain the fGn

607 result: $\approx t^{2\alpha-1}$. For pure fRn processes this reduces to $R_{0,h}(t) = -\frac{1}{\Gamma(-h)} t^{-1-h}$ (note that $\Gamma(-h)$

608 <0 for $0<h<1$).
609   Integrating $R_{\alpha,h}$ twice, we obtain

610
$$V_{\alpha,h}(t) = \frac{2\Gamma(-1-2\alpha)\sin(\pi\alpha)}{\pi}t^{1+2\alpha} + a_{\alpha,h}t + b_{\alpha,h} - \frac{1+\cos(\pi h)-\sin(\pi h)\cot(\pi(h-2\alpha))}{\Gamma(2-(h-2\alpha))}t^{1+2\alpha-h} + ...; \quad t \gg 1$$

611
$$(56)$$

612 (the full expansion is given in appendix A, see fig. 3 for plots). The constants of integration
613 $a_{\alpha,h}$, $b_{\alpha,h}$ are not determined since the expansion is not valid at $t = 0$; they can be determined
614 numerically if needed. However, in the limit $\alpha \to 0$ (the pure fRn case), the leading term is
615 exactly t (corresponding to ordinary Brownian motion) so that an extra $a_{0,h}$ is not needed
616 (appendix A). When $\alpha > 0$, the far left (fGn) term from the forcing dominates, at large
617 enough t, $V_{\alpha,h}(t) \propto t^{2H}$ with $H = \alpha + 1/2$, the corresponding motion is an fBm.

618 Using the above results we see that there are three limiting fRn/fRm cases that yield
619 fGn/fBm processes:

620
$$R_{\alpha,0}(t) = \frac{1}{4}R_\alpha^{(fGn)}(t); \qquad 0 < \alpha < 1/2; \qquad h = 0$$
$$R_{\alpha,h}(t) = R_\alpha^{(fGn)}(t); \qquad 0 < \alpha < 1/2; \qquad t \gg 1 \qquad\qquad (57)$$
$$R_{\alpha,h}(t) = R_{\alpha+h}^{(fGn)}(t); \qquad 0 < \alpha + h < 1/2; \quad t \approx 0$$
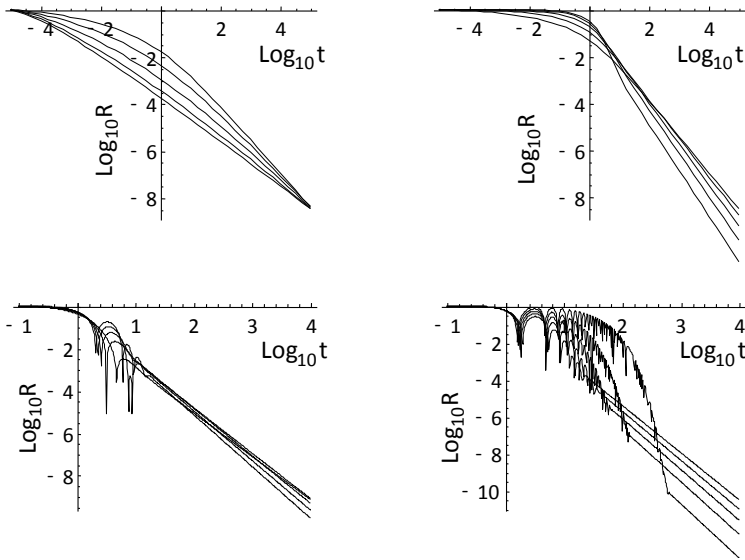
621
622
623 Fig. 2: The normalized correlation functions $R_{0,h}$ for fRn corresponding to the $V_{0,h}$ function
624 in fig. 2: $0 < h < 1/2$ (upper left) $1/2 < h < 1$ (upper right), $1 < h < 3/2$) lower left, $3/2 < h < 2$ lower

625 right.   In each plot, the curves correspond to h increasing from bottom to top in units of 1/10
626 starting from 1/20 (upper left) to 39/20 (bottom right). For $h<1/2$, the resolution is important since

627 $R_{0,h,\tau}$ diverges at small τ. In the upper left figure, $R_{0,h,\tau}$ is shown with $\tau = 10^{-5}$; they were

628 normalized to the value at resolution $\tau = 10^{-5}$, for $h > 1/2$, the curves are normalized with $F_3^{-1/2}$.   In

629 all cases, the large t slope is $- 1-h$.
630
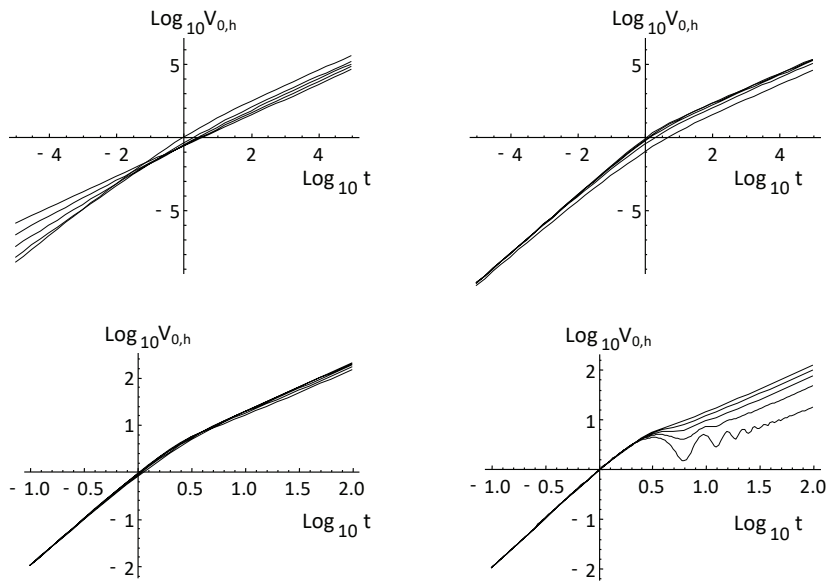
631
632 Fig. 3: The normalized $V_{0,h}$ functions for the various ranges of h for fRm. The plots from
633 left to right, top to bottom are for the ranges $0 < h < 1/2$, $1/2 < h < 1$, $1 < h < 3/2$, $3/2 < h < 2$. Within
634 each plot, the lines are for h increasing in units of 1/10 starting at a value 1/20 above the plot
635 minimum; overall, h increases in units of 1/10 starting at a value 1/20, upper left to 39/20,
636 bottom right (ex. for the upper left, the lines are for $h = 1/20, 3/10, 5/20, 7/20, 9/20$). For all h's
637 the large t behaviour is linear (slope = 1, although note the oscillations for the lower right hand plot
638 for $3/2<h<2$). For small t, the slopes are $1+2h$ ($0<h\leq1/2$) and 2 ($1/2\leq h<2$).
639

640 **3.3 Haar fluctuations**
641   A useful statistical characterization of the processes is by the statistics of their Haar
642 fluctuations over an interval Δt. For an interval Δt, Haar fluctuations (based on Haar
643 wavelets) are the differences between the averages of the first and second halves of an
644 interval. For a process U, the Haar fluctuation is:

645
$$\Delta U\left(\Delta t\right)_{Haar} = \frac{2}{\Delta t}\int_{t-\Delta t/2}^{t} U\left(v\right)dv - \frac{2}{\Delta t}\int_{t-\Delta t}^{t-\Delta t/2} U\left(v\right)dv .$$
(58)

646 In terms of the process at resolution $\Delta t/2$, (i.e. averaged at this scale) $U_{\Delta t/2}\left(t\right)$:

647
$$\Delta U\left(\Delta t\right)_{Haar} = \frac{2}{\Delta t}\left(U_{\Delta t/2}\left(t\right) - U_{\Delta t/2}\left(t-\Delta t/2\right)\right) .$$
(59)

648 Therefore:

649
$$\left\langle \Delta U\left(\Delta t\right)_{Haar}^{2}\right\rangle = \left(\frac{2}{\Delta t}\right)^{2}\left(4V\left(\Delta t/2\right) - V\left(\Delta t\right)\right) .$$
(60)

650 Where $V(t)$ is the variance of the integral of U over an interval t (eq. 34).

651 Using eq. 60 we can determine the behaviour of the RMS Haar fluctuations; terms

652 like $V_{\alpha,h}\left(t\right) \propto t^{\xi}$ contribute $\propto t^{\xi/2-1}$ to the RMS Haar fluctuation $\left\langle \Delta U_{\alpha,h}\left(\Delta t\right)_{Haar}^{2}\right\rangle^{1/2}$ (the

653 exception is when $\xi = 2$ which contributes nothing). Applying this equation to fGn

654 parameter h we obtain $\left\langle \Delta F_{h}\left(\Delta t\right)_{Haar}^{2}\right\rangle^{1/2} \propto \Delta t^{H}$ with $H = h - \frac{1}{2}$.

655 Using the results above for $V_{\alpha,h}$ we therefore obtain the leading exponents:

$$
\begin{aligned}
H &= h+\alpha-1/2; \quad 0<h+\alpha<3/2 \\
H &= 1; \qquad\qquad 3/2<h+\alpha<2
\end{aligned} \;;\quad \Delta t \ll 1
$$

$$H = \alpha - \frac{1}{2}; \quad \Delta t \gg 1$$

656
(61)

657 Fig. 4 shows that the theory agrees well with the numerics.

658 For the range of α, h discussed here ($0\le\alpha<1/2$, $0\le h\le 2$), H spans the range -1/2 (white
659 noise) to 1. In comparison, fGn processes have H covering the range $-1 < H < 0$ and fBm
660 processes have $0<H<1$, therefore, depending on whether the process is observed at time
661 scales below or above the relaxation time scale ($\Delta t = 1$), fractionally integrated fRn
662 processes can mimic fGn or fBm processes. If we consider the integrals - the motions -
663 the value of H is increased by 1 (although for Haar fluctuations, it cannot exceed $H = 1$).
664 Overall, from an empirical viewpoint, if over some range of scales (that may only be a
665 factor of 100 or less), it may be quite hard to distinguish the various models, especially
666 since the transition from low to high frequency scaling may be very slow (see especially
667 appendix B for the $h = 1/2$ case). Recent work shows that the maximum likelihood method
668 may be the optimum parameter estimation technique [Procyk, 2021].
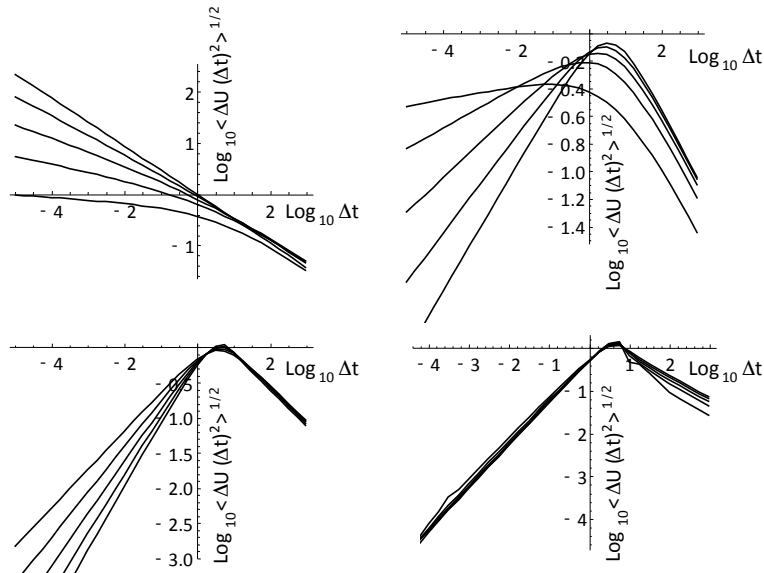
669
670   Fig. 4: The RMS Haar fluctuation plots for the pure ($\alpha = 0$) fRn process for $0 < h < 1/2$
671 (upper left), $1/2 < h < 1$ (upper right), $1 < h < 3/2$ (lower left), $3/2 < h < 2$ (lower right). The
672 individual curves correspond to those of fig. 2, 3. The small Δt slopes follow the theoretical
673 values $h - 1/2$ up to $h = 3/2$ (slope= 1); for larger h, the small t slopes all = 1. Also, at large t
674 due to dominant $V \approx t$ terms, in all cases we obtain slopes $t^{-1/2}$.

675 **3.4 Sample processes**
676   It is instructive to view some samples of fRn, fRm processes, (here we consider only
677 $\alpha = 0$). For simulations, both the small and large scale divergences must be considered.
678 Starting with the approximate methods developed by [*Mandelbrot and Wallis*, 1969], it
679 took some time for exact fBm, and fGn simulation techniques to be developed [*Hipel and*
680 *McLeod*, 1994], [*Palma*, 2007]. Fortunately, for fRm, fRn, the low frequency situation is
681 easier since the long time memory is much smaller than for fBm, fGn. Therefore, as long
682 as we are careful to always simulate series a few times longer than the relaxation time and
683 then to throw away the earliest 2/3 or 3/4 of the simulation, the remainder will have accurate
684 statistics. With this procedure to take care of low frequency issues, we can therefore use
685 the solution for fRn in the form of a convolution, and use standard numerical convolution
686 algorithms.
687   We must nevertheless be careful about the high frequencies since the impulse
688 response Green's functions $G_{0,h}$ are singular for $h<1$. In order to avoid singularities,
689 simulations of fRn are best made by first simulating the motions $Q_{0,h}$ using $Q_{0,h} \propto G_{1,h} * \gamma$

690 and obtain the resolution τ fRn, using $U_{0,h,\tau}(t) = \left(Q_{0,h}(t+\tau) - Q_{0,h}(t)\right)/\tau$. Numerically,
691 this allows us to use the smoother (nonsingular) $G_{1,h}$ in the convolution rather than the
692 singular $G_{0,h}$. The simulations shown in figs. 5, 6 follow this procedure and the Haar
693 fluctuation statistics were analyzed verifying the statistical accuracy of the simulations.
694   In order to clearly display the behaviours, recall that when $t \gg 1$, we showed that all
695 the fRn converge to Gaussian white noises and the fRm to Brownian motions (albeit in a
696 slow power law manner). At the other extreme, for $t \ll 1$, we obtain the fGn and fBm
697 limits (when $0 < h < 1/2$) and their generalizations for $1/2 < h < 2$.
698   Fig. 5a shows three simulations, each of length 2^{19}, pixels, with each pixel
699 corresponding to a temporal resolution of $\tau = 2^{-10}$ so that the unit (relaxation) scale is 2^{10}
700 elementary pixels. Each simulation uses the same random seed but they have h's increasing
701 from $h = 1/10$ (top set) to $h = 5/10$ (bottom set). The fRm at the right is from the running
702 sum of the fRn at the left. Each series has been rescaled so that the range (maximum -
703 minimum) is the same for each. Starting at the top line of each group, we show 2^{10} points
704 of the original series degraded by a factor 2^9. The second line shows a blow-up by a factor
705 of 8 of the part of the upper line to the right of the dashed vertical line. The line below is
706 a further blown up by factor of 8, until the bottom line shows 1/512 part of the full
707 simulation, but at full resolution. The unit scale indicating the transition from small to
708 large is shown by the horizontal red line in the middle right figure. At the top (degraded
709 by a factor 2^9), the unit (relaxation) scale is 2 pixels so that the top line degraded view of
710 the simulation is nearly a white noise (left), (ordinary) Brownian motion (right). In contrast,
711 the bottom series is exactly of length unity so that it is close to the fGn limit with the
712 standard exponent $H = h+1/2$. Moving from bottom to top in fig. 5a, one effectively
713 transitions from fGn to fRn (left column) and fBm to fRm (right).
714   If we take the empirical relaxation scale for the global temperature to be 2^7 months
715 (≈ 10 years, [*Lovejoy et al.*, 2017]) and we use monthly resolution temperature anomaly
716 data, then the nondimensional resolution is 2^{-7} corresponding to the second series from the
717 top (which is thus 2^{10} months ≈ 80 years long). Since $h \approx 0.42 \pm 0.02$ ([*Del Rio Amador and
718 Lovejoy*, 2019]), the second series from the top in the bottom set is the most realistic, we
719 can make out the low frequency ondulutions that are mostly present at scales 1/8 of the
720 series (or less).
721   Fig. 5b shows realizations constructed from the same random seed but for the
722 extended range $1/2 < h < 2$ (i.e. beyond fGn). Over this range, the top (large scale,
723 degraded resolution) series is close to a white noise (left) and Brownian motion (right). For
724 the bottom series, there is no equivalent fGn or fBm process, the curves become smoother
725 although the rescaling may hide this somewhat (see for example the $h = 13/20$ set, the blow-
726 up of the far right 1/8 of the second series from the top shown in the third line. For $1 < h$
727 < 2, also note the oscillations with frequency $2\pi / \sin(\pi / h)$ (eq. 49), this is the fractional
728 oscillation range.
729   Fig. 6a shows simulations similar to fig. 5a (fRn on the left, fRm on the right) except
730 that instead of making a large simulation and then degrading and zooming, all the
731 simulations were of equal length (2^{10} points), but the relaxation scale was changed from
732 2^{15} pixels (bottom) to 2^{10}, 2^5 and 1 pixel (top). Again the top is white noise (left), Brownian
733 motion (right), and the bottom is (nearly) fGn (left) and fBm (right), fig. 6b shows the
734 extensions to $1/2 < h < 2$.

735
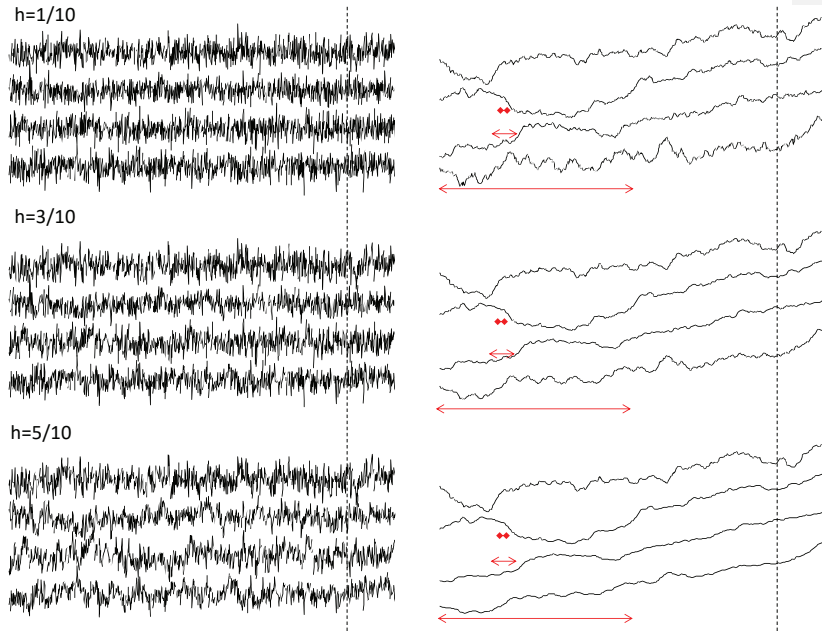
h=1/10

h=3/10

h=5/10

736
737   Fig. 5a: fRn and fRm simulations (left and right columns respectively) for h = 1/10, 3/10,
738 5/10 (top to bottom sets, all with $\alpha = 0$) i.e. the exponent range that overlaps with fGn and fBm.
739 There are three simulations, each of length 2^{19} pixels, each use the same random seed with the unit
740 scale equal to 2^{10} pixels (i.e. a resolution of $\tau = 2^{-10}$). The entire simulation therefore covers the
741 range of scale 1/1024 to 512 units. The fRm at the right is from the running sum of the fRn at the
742 left.
743   Starting at the top line of each set, we show 2^{10} points of the original series degraded in
744 resolution by a factor 2^9. Since the length is $t = 2^9$ units long, each pixel has resolution $\tau = 1/2$).
745 The second line of each set takes the segment of the upper line lying to the right of the dashed
746 vertical line, 1/8 of its length. It therefore spans t=0 to $t = 2^9/8 = 2^6$ but resolution was taken as $\tau =$
747 2^{-4}, hence it is still 2^{10} pixels long. Since each pixel has a resolution of 2^{-4}, the unit scale is 2^4 pixels
748 long, this is shown in red in the second series from the top (middle set). The process of taking 1/8
749 and blowing up by a factor of 8 continues to the third line (length $t = 2^3$, resolution $\tau = 2^{-7}$), unit
750 scale =2^7 pixels (shown by the red arrows in the third series) until the bottom series which spans
751 the range $t = 0$ to $t = 1$ and a resolution $\tau = 2^{-10}$ with unit scale 2^{10} pixels (the whole series displayed).
752 Each series was rescaled in the vertical so that its range between maximum and minimum was the
753 same.
754   The unit relaxation scales indicated by the red arrows mark the transition from small to large
755 scale. Since the top series in each set has a unit scale of 2 (degraded) it is nearly a white noise (left),
756 or (ordinary) Brownian motion (right). In contrast, the bottom series is exactly of length $t = 1$ so
757 that it is close to the fGn and fBm limits (left and right) with the standard exponent $H = h +1/2$. As
758 indicated in the text, the second series from the top in the bottom set is most realistic for monthly
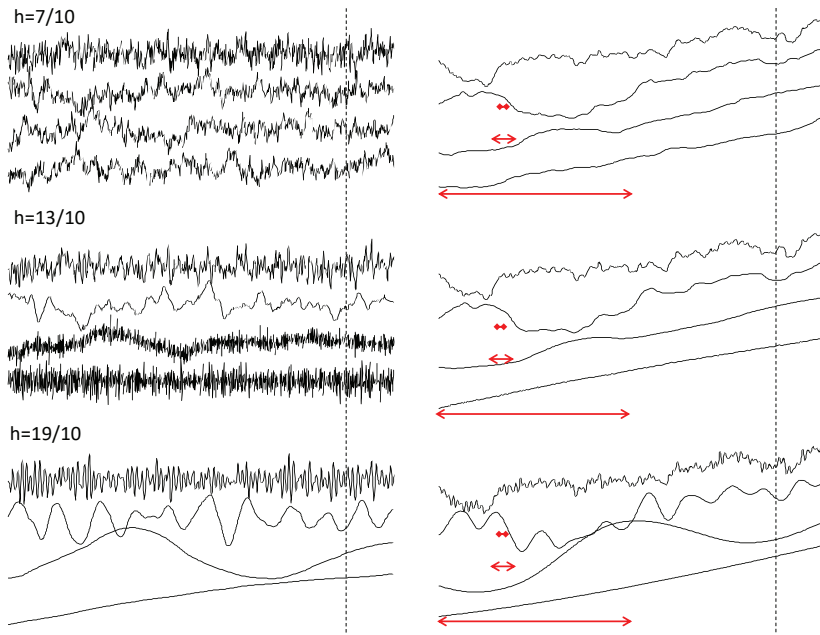759 temperature anomalies.

760
761

762
763   Fig. 5b: The same as fig. 5a but for h = 7/10, 13/10 and 19/10 (top to bottom). Over this
764 range, the top (large scale, degraded resolution) series is close to a white noise (left) and Brownian
765 motion (right). For the bottom series, there is no equivalent fGn or fBm process, the curves become
766 smoother although the rescaling may hide this somewhat (see for example the middle h = 13/20 set,
767 the blow-up of the far right 1/8 of the second series from the top shown in the third line). Also note
768 for the bottom two sets with $1 < h < 2$, the oscillations that have frequency $2\pi / \sin(\pi / h)$, this is
769 the fractional oscillation range.
770
771

h=1/10

h=3/10

h=5/10
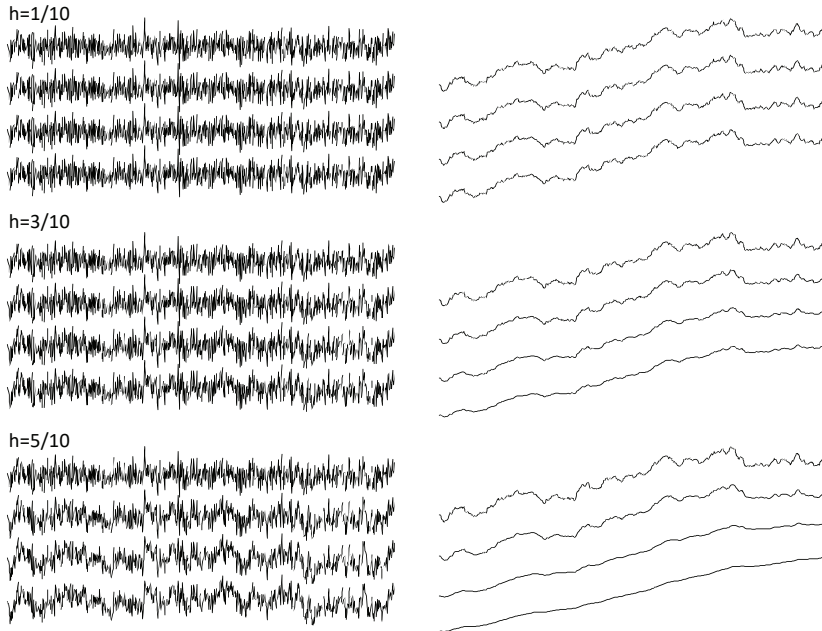
772
773   Fig. 6a: This set of simulations is similar to fig. 5a (fRn on the left, fRm on the right) except
774 that instead of making a large simulation and then degrading and zooming, all the simulations were
775 of equal length (2^{10} points), but resolutions $\tau = 2^{-15}$, 2^{-10}, 2^{-5}, 1 (bottom to top). The simulations
776 therefore spanned the ranges of scale 2^{-15} to 2^{-5} ; 2^{-10} to 1 ; 2^{-5} to 2^{5} ; 1 to 2^{10} and the same random
777 seed was used in each so that we can see how the structures slowly change when the relaxation
778 scale changes. The bottom fRn, $h= 5/10$ set is the closest to that observed for the Earth's
779 temperature, and since the relaxation scale is of the order of a few years, the second series from the
780 top of this set (with one pixel = one month) is close to that of monthly global temperature anomaly
781 series. In that case the relaxation scale would be 32 months and the entire series would be $2^{10}/12 \approx$
782 85 years long.
783   The top series (of total length 2^{10} relaxation times) is (nearly) a white noise (left), and
784 Brownian motion (right), and the bottom is (nearly) an fGn (left) and fBm (right). The total range
785 of scales covered here (2^{10}x2^{15}) is larger than in fig. 5a and allows one to more clearly distinguish
786 the high and low frequency regimes.
787

h=7/10

h=13/10

h=19/10
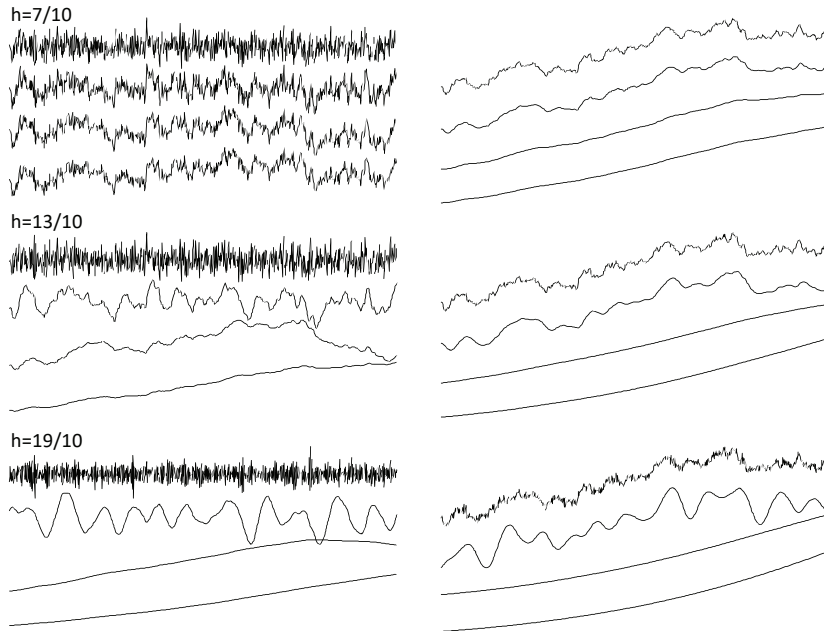
788
789   Fig. 6b: The same fig. 6a but for larger *h* values; see also fig. 5b.

790   **4. Prediction**

791   The initial value for Weyl fractional differential equations is effectively at $t = -\infty$,
792   so that for fRn, it is not directly relevant at finite times (although the ensemble mean is
793   assumed = 0; for fRm, the initial condition $Q_{\alpha,h}(0) = 0$ is important).   The prediction
794   problem is thus to use past data (say, for $t < 0$) in order to make the most skillful prediction
795   for $t > 0$.   We are therefore dealing with a *past value* rather than a usual *initial value*
796   problem. The emphasis on past values is particularly appropriate since in the fGn limit,
797   the memory is so large that values of the series in the distant past are important. Indeed,
798   prediction of fGn with a finite length of past data involves placing strong (mathematically
799   singular) weights on the most ancient data available (see [*Gripenberg and Norros*, 1996],
800   [*Del Rio Amador and Lovejoy*, 2019], [*Del Rio Amador and Lovejoy*, 2021a], [*Del Rio
801   Amador and Lovejoy*, 2021b]). This is quite different from standard stochastic predictions
802   that are based on short memory (exponential) auto-regressive or moving average type
803   processes that are not much different from initial value problems.
804   To deal with the small scale divergences when $0 < h+\alpha \leq 1/2$ it is necessary to
805   predict the finite resolution fRn: $U_{\alpha,h,\tau}(t)$. Using eq. 40 for $U_{\alpha,h,\tau}(t)$, we have:

$$U_{\alpha,h,\tau}(t) = \frac{1}{\tau}\left[\int_{-\infty}^{t}G_{1+\alpha,h}(t-v)\gamma(v)dv - \int_{-\infty}^{0}G_{1+\alpha,h}(-v)\gamma(v)dv\right] -$$

$$\frac{1}{\tau}\left[\int_{-\infty}^{t-\tau}G_{1+\alpha,h}(t-\tau-v)\gamma(v)dv - \int_{-\infty}^{0}G_{1+\alpha,h}(-v)\gamma(v)dv\right] . \quad (62)$$

$$= \frac{1}{\tau}\left[\int_{-\infty}^{t}G_{1+\alpha,h}(t-v)\gamma(v)dv - \int_{-\infty}^{t-\tau}G_{1+\alpha,h}(t-\tau-v)\gamma(v)dv\right]$$

Now define the predictor for $t \geq 0$ (indicated by a circonflex):

$$\widehat{U_{\alpha,h,\tau}}(t) = \frac{1}{\tau}\left[\int_{-\infty}^{0}G_{1+\alpha,h}(t-v)\gamma(v)dv - \int_{-\infty}^{0}G_{1+\alpha,h}(t-\tau-v)\gamma(v)dv\right]. \quad (63)$$

To show that it is indeed the optimal predictor, consider the predictor error $E_{\tau}(t)$:

$$E_{\tau}(t) = U_{\alpha,h,\tau}(t) - \widehat{U_{\alpha,h,\tau}}(t) = \tau^{-1}\left[\int_{-\infty}^{t}G_{1+\alpha,h}(t-v)\gamma(v)dv - \int_{-\infty}^{t-\tau}G_{1+\alpha,h}(t-\tau-v)\gamma(v)dv\right]$$

$$-\tau^{-1}\left[\int_{-\infty}^{0}G_{1+\alpha,h}(t-v)\gamma(v)dv - \int_{-\infty}^{0}G_{1+\alpha,h}(t-\tau-v)\gamma(v)dv\right] .$$

$$= \tau^{-1}\left[\int_{0}^{t}G_{1+\alpha,h}(t-v)\gamma(v)dv - \int_{0}^{t-\tau}G_{1+\alpha,h}(t-\tau-v)\gamma(v)dv\right]$$

$$(64)$$

Eq. 64 shows that the error depends only on $\gamma(v)$ for $v>0$ whereas the predictor (eq. 63) only depends on $\gamma(v)$ for $v<0$, hence they are orthogonal:

$$\left\langle E_{\tau}(t)\widehat{U_{\alpha,h,\tau}}(t)\right\rangle = 0, \quad (65)$$

this is a sufficient condition for $\widehat{U_{\alpha,h,\tau}}(t)$ to be the minimum square predictor which is the optimal predictor for stationary Gaussian processes, (e.g. [*Papoulis*, 1965]). The prediction error variance is:

$$\left\langle E_{\tau}(t)^{2}\right\rangle = \tau^{-2}\left[\int_{0}^{t-\tau}\left(G_{1+\alpha,h}(t-v) - G_{1+\alpha,h}(t-\tau-v)\right)^{2}dv + \int_{t-\tau}^{t}G_{1+\alpha,h}(t-v)^{2}dv\right],$$

$$(66)$$

or with a change of variables:

$$\left\langle E_{\tau}(t)^{2}\right\rangle = \tau^{-2}V_{\alpha,h}(\tau) - \tau^{-2}\left[\int_{t-\tau}^{\infty}\left(G_{1+\alpha,h}(v+\tau) - G_{1+\alpha,h}(v)\right)^{2}dv\right], \quad (67)$$

where we have used $\left\langle U_{\alpha,h,\tau}^{2}\right\rangle = \tau^{-2}V_{\alpha,h}(\tau)$ (the unconditional variance).

Using the usual definition of forecast skill (also called the "Minimum Square Skill Score" or "MSSS") we obtain:

$$S_{k,\tau}(t) = 1 - \frac{\left\langle E_\tau(t)^2 \right\rangle}{\left\langle E_\tau(\infty)^2 \right\rangle} = \frac{\int\limits_{t-\tau}^{\infty} \left(G_{1+\alpha,h}(u+\tau) - G_{1+\alpha,h}(u)\right)^2 du}{V_{\alpha,h}(\tau)}$$

$$= \frac{\int\limits_{t-\tau}^{\infty} \left(G_{1+\alpha,h}(v+\tau) - G_{1+\alpha,h}(v)\right)^2 dv}{\int\limits_{0}^{\infty} \left(G_{1+\alpha,h}(v+\tau) - G_{1+\alpha,h}(v)\right)^2 dv + \int\limits_{0}^{\tau} G_{1+\alpha,h}(v)^2 dv}$$

. (68)

When $h < 1/2$ and $G_{1,h}(t) = G_{1,h}^{(fGn)}(t) = \dfrac{t^h}{\Gamma(1+h)}$, we obtain the fGn result:

$$S_k = \frac{\xi_h(\infty) - \xi_h(\lambda)}{\xi_h(\infty) + \dfrac{1}{2h+1}} \qquad\qquad \xi_h(\lambda) = \int\limits_0^{\lambda-1} \left((v+1)^h - v^h\right)^2 dv \qquad (69)$$

[*Lovejoy et al.*, 2015]. Where λ is the forecast horizon (lead time) measured in the number of time steps in the future (due to the fGn scaling, it is independent of the resolution τ). The MSSS gives the fraction of the variance explained by the optimum predictor, when the skill = 1, the forecast is perfect.

To survey the implications, let's start by showing the τ independent results for fGn, shown in fig. 7 which is a variant on a plot published in [*Lovejoy et al.*, 2015]. We see that when $h \approx 1/2$ ($H \approx 1$) that the skill is very high, indeed, in the limit $h \rightarrow 1/2$, we have perfect skill for fGn forecasts (this would of course require an infinite amount of past data to attain).
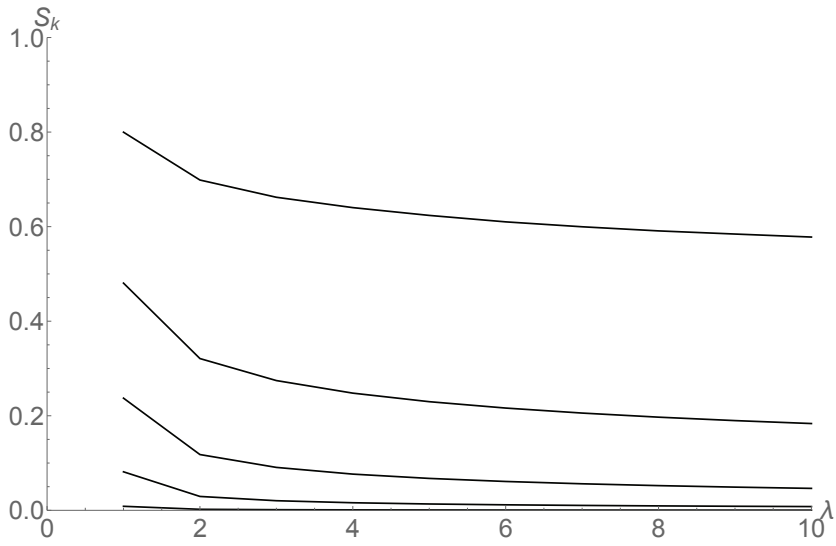
Fig. 7: The prediction skill (S_k) for pure fGn processes for forecast horizons up to $\lambda = 10$ steps (ten times the resolution). This plot is non-dimensional, it is valid for time steps of any duration. From bottom to top, the curves correspond to $h = 1/20$, $3/10$, …$9/20$ (red, top, close to the empirical h).
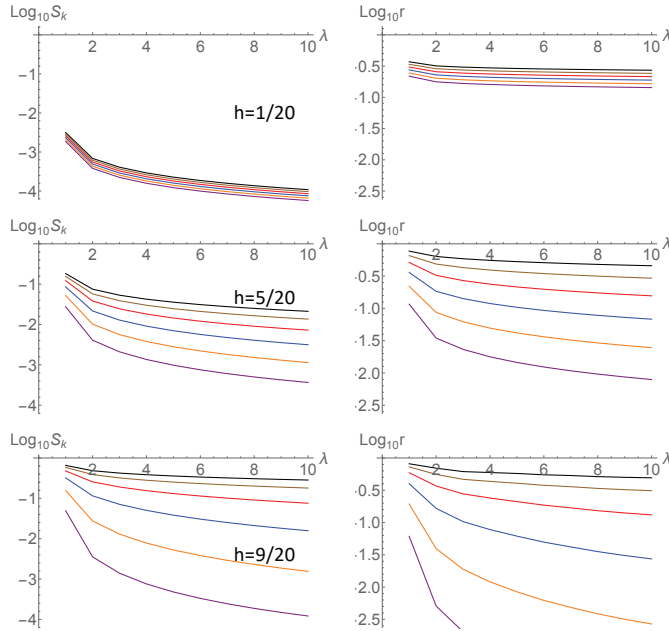
844
845   Fig. 8: The left column shows the skill (S_k) of pure ($\alpha = 0$) fRn forecasts (as in fig. 7 for
846 fGn) for fRn skill with $h = 1/20$, 5/20, 9/20 (top to bottom set); λ is the forecast horizon, the number
847 of steps of resolution τ forecast into the future. The right hand column shows the ratio (r) of the
848 fRn to corresponding fGn skill.
849   Here the result depends on τ; each curve is for different values increasing from 10^{-4} (top,
850 black) to 10 (bottom, purple) increasing by factors of 10 (the red set in the bottom plots with $\tau =$
851 10^{-2}, $h = 9/20$ are closest to the empirical values).
852
853   Now consider the fRn skill, we'll start by considering the pure ($\alpha = 0$) fRn case where
854 the memory comes completely from the (high frequency) storage, anticipating that the fGn
855 forced case ($\alpha \neq 0$) obtains its memory and skill from both storage and the forcing. In
856 comparison with fGn, fRn has an extra parameter, the resolution of the data, τ. Figure 8
857 shows curves corresponding to fig. 7 for fRn with forecast horizons integer multiples (λ)
858 of τ i.e. for times $t = \lambda\tau$ in the future, but with separate curves, one for each of five τ values
859 increasing from 10^{-4} to 10 by factors of ten. When τ is small, the results should be close to
860 those of fGn, i.e. with potentially high skill, and in all cases, the skill is expected to vanish
861 quite rapidly for $\tau > 1$ since in this limit, fRn becomes an (unpredictable) white noise
862 (although there are scaling corrections to this).
863   To better understand the fGn limit, it is helpful to plot the ratio of the fRn to fGn skill
864 (fig. 8, right column). We see that even with quite small values $\tau = 10^{-4}$ (top, black curves),
865 that some skill has already been lost. Fig. 9 shows this more clearly, it shows one time step
866 and ten time step skill ratios. To put this in perspective, it is helpful to compare this using

867 some of the parameters relevant to macroweather forecasting. According to [*Lovejoy et al.*,
868 2015] and [*Del Rio Amador and Lovejoy*, 2019], the relevant empirical Haar exponent is ≈
869 -0.08 for the global temperature so that h = 1/2 - 0.08 ≈ 0.42. Although direct empirical
870 estimates of the relaxation time, are difficult since the responses to anthropogenic forcing
871 begin to dominate over the internal variability after ≈10 years [*Procyk et al.*, 2020] have
872 used the deterministic response to estimate a global relaxation time of ≈ 5 years (work in
873 progress using maximum likelihood estimates shows that a scales of hundreds of kilometers,
874 it is quite variable ranging from months to decades [*Procyk*, 2021]). For monthly resolution
875 forecasts, the non-dimensional resolution is τ ≈ 1/100. With these values, we see (red
876 curves) that we may have lost ≈ 30% of the fGn skill for one month forecasts and ≈ 85%
877 for ten month forecasts. Comparing this with fig. 7 we see that this implies about 60% and
878 10% skill (see also the red curve in fig. 8, bottom set).
879   Going beyond the $0 < h < 1/2$ region that overlaps fGn, fig. 9, 10 clearly shows that
880 the skill continues to increase with h. We already saw (fig. 4) that the range $1/2 < h < 3/2$
881 has RMS Haar fluctuations that for $\Delta t < 0$ mimic fBm and these do indeed have higher skill,
882 approaching unity for h near 1 corresponding to a Haar exponent ≈ 1/2, i.e. close to an fBm
883 with H = 1/2, i.e. a regular Brownian motion. Recall that for Brownian motion, the
884 increments are unpredictable, but the process itself is predictable (persistence). In figure
885 9, we show the skill for various h's as a function of resolution τ. Fig. 11a shows that for h
886 < 3/2, the skill decreases rapidly for $\tau > 1$. Fig. 11b in the fractional oscillation equation
887 regime shows that the skill oscillates.
888   We may now consider the skill of the fGn forced process ($\alpha \neq 0$), fig. 12. For small
889 τ, short lags, λ (the upper left), the contours are fairly linear along lines of constant $h+\alpha$,
890 so that as expected, the predictability is essentially that of an fGn process but with effective
891 exponent $h+\alpha$. At the opposite extreme (large τ, h, the lines are fairly horizontal, indicating
892 that the skill from the storage (i.e. from h) is negligible, and that all the memory (and hence
893 skill) comes from the forcing fGn, exponent α. The in-between resolutions and lags
894 generally have in-between slopes. As expected, the skill from the storage drops off quickly
895 for resolutions ≈> τ. For $h{\geq}1$, there is some waviness in the contours due to the oscillatory
896 nature of the Green's functions.
897
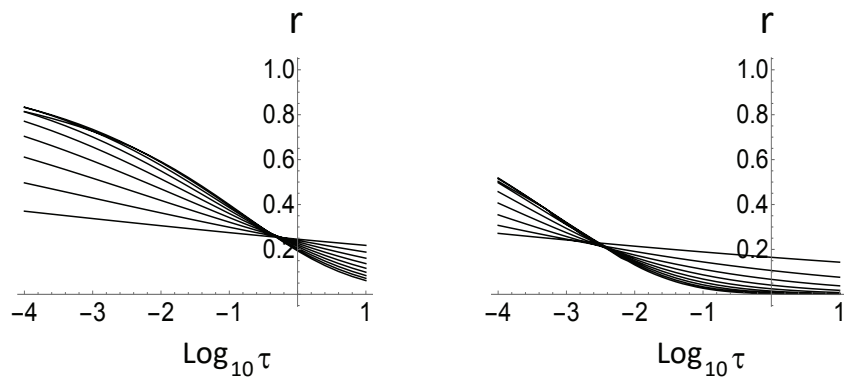
898
899   Fig. 9: The ratio of ($\alpha = 0$) fRn skill to fGn skill (left: one step horizon, right: ten step
900   forecast horizon) as a function of resolution τ for h increasing from (at left) bottom to top ($h = 1/20$,
901   2/20, 3/20…9/20); the $h = 9/20$ curves (close to the empirical value) is the curve that starts at the
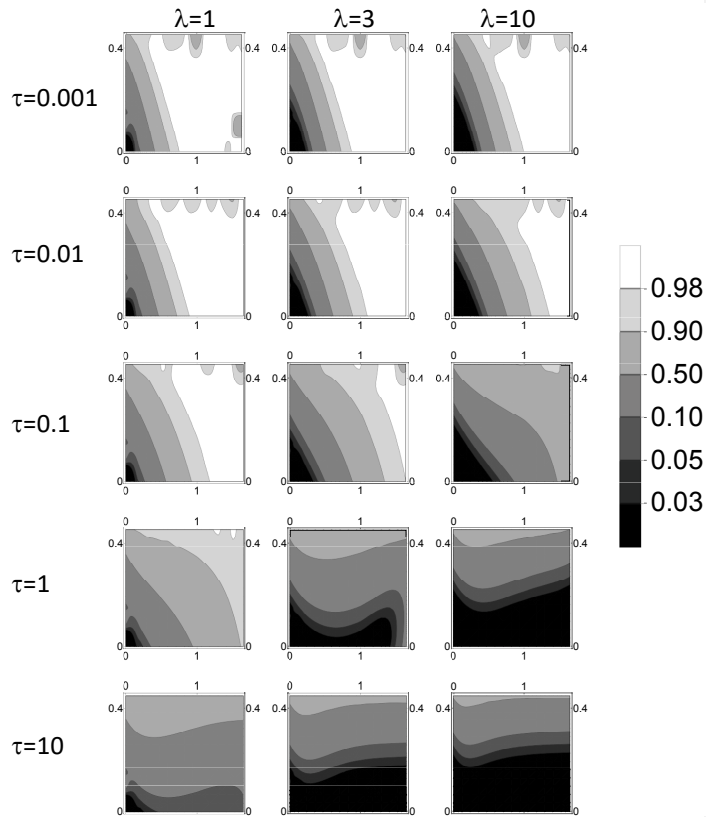902   left of each plot.
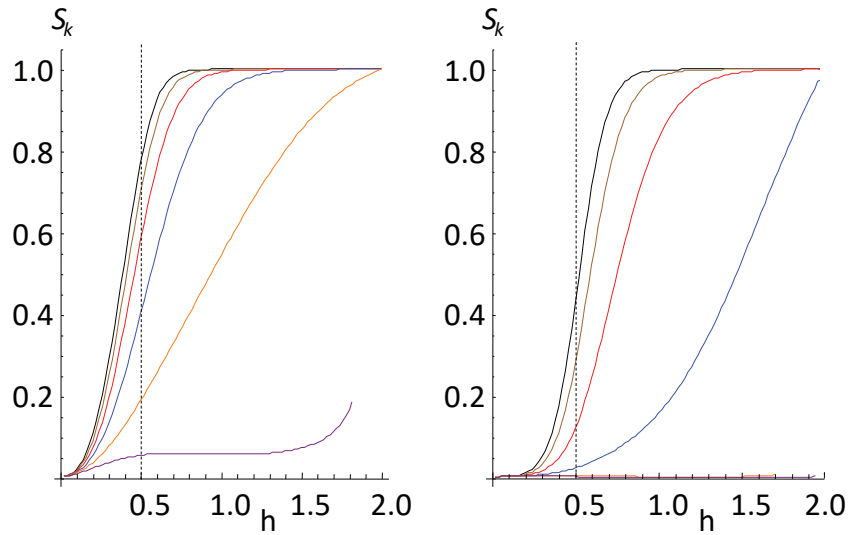
903
904 Fig. 10: The one step (left) and ten step (right) pure ($\alpha = 0$) fRn forecast skill as a function
905 of h for various resolutions (τ) ranging from $\tau = 10^{-4}$ (black, left of each set) through $\tau = 10^{-3}$
906 (brown) 10^{-2} (red), 0.1 (blue), 1 (orange), 10 (purple). In the right set $\tau = 1$ (orange), 10 (purple)
907 lines are nearly on top of the $S_k = 0$ line. Again red ($\tau = 10^{-2}$) is the more empirical relevant value
908 for monthly data. Recall that the regime $h < 1/2$ (to the left of the vertical dashed lines) corresponds
909 to the overlap with fGn.
910
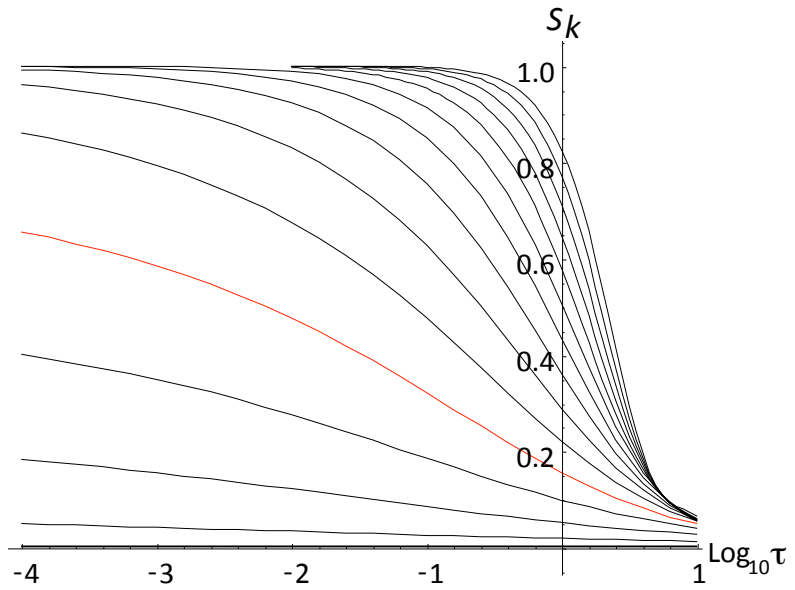
911
912   Fig. 11a: One step pure ($\alpha = 0$) fRn prediction skills as a function of resolution for h's
913   increasing from 1/20 (bottom) to 29/20 (top), every 1/10. Note the rapid transition to low skill,
914   (white noise) for $\tau > 1$. The curve for $h = 9/20$ is shown in red.
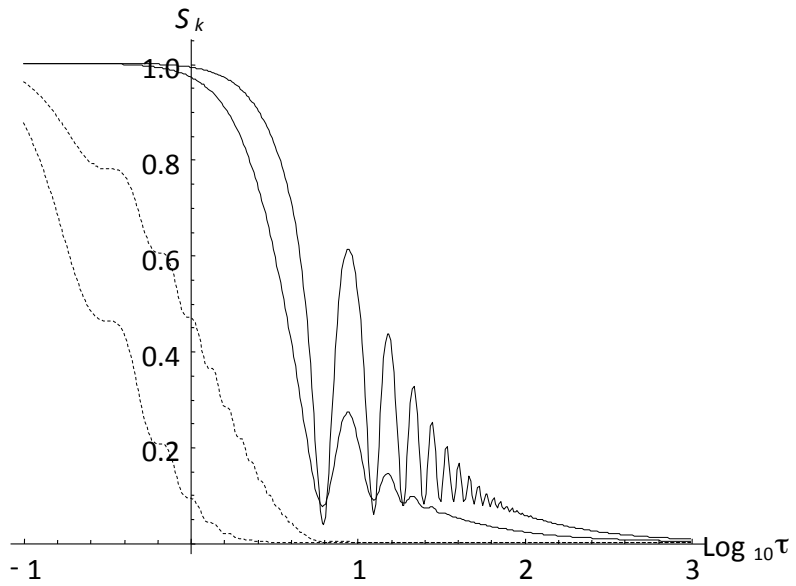
915
916   Fig. 11b: Same as fig. 11a except for $h = 37/20$, $39/20$ showing the one step skill (black),
917 and the ten step skill (dashed). The right hand dashed and right hand solid lines, are for $h = 39/20$,
918 they clearly show that the skill oscillates in this fractional oscillation equation regime. The
919 corresponding left lines are for $h = 37/20$.

Fig. 12: Contour plots of the forecast skill, with *h* along the horizontal and α along the vertical axis. The plots are for increasing nondimensional resolutions: τ = 0.001, 0.01, 0.1, 1, 10 (top to bottom), with forecasts for lags λ = 1, 3, 10 (left to right) and with contour levels (legend) varying from nearly no skill (0.03), to nearly full skill (0.98).

4. Conclusions:

Ever since [*Budyko*, 1969] and [*Sellers*, 1969], the energy balance between the earth and outer space has been modelled by the Energy Balance Equation (EBE), based on the continuum heat equation, see [*North and Kim*, 2017] for a recent review and see [*Ziegler and Rehfeld*, 2020] for a recent regional application). It is most commonly used as a model for the globally averaged temperature where it is usually derived by applying Newton's law of cooling applied to a uniform slab of material, a "box". The resulting EBE is a first order relaxation equation describing the exponent relaxation of the temperature to a new equilibrium after it has been perturbed by an external forcing. Its first order ($h = 1$) derivative term accounts for energy storage.

935   The resulting model relaxes to equilibrium much too quickly so that to increase
936 realism, it is usual to introduce a few interacting slabs (representing for example the
937 atmosphere and ocean mixed layer; the Intergovernmental Panel on Climate Change
938 recommends two such components [*IPCC*, 2013]). However, it turns out that these $h = 1$
939 box models do not use the correct surface radiative-conductive boundary conditions. If
940 one assumes heat transport by the classical heat equation and these boundary conditions
941 are used instead, one instead obtains the Half-order EBE, the HEBE with $h = 1/2$ [*Lovejoy*,
942 2021a; b] which is already close to the global empirical value ($h = 0.42\pm0.03$, [*Del Rio*
943 *Amador and Lovejoy*, 2019], see also [*Lovejoy et al.*, 2015]). However this model is only
944 valid in the macroweather regime - for time scales of weeks and longer and due to the
945 spatial scaling in the atmosphere, the fractional heat equation (FHE) may be more a more
946 appropriate model than the classical one. The use of the FHE can be justified by
947 recognizing that a realistic energy transport model involves a continuous hierarchy of
948 mechanisms. The extension to the FHE leads directly to a fractional relaxation equation
949 that generalizes the EBE: the Fractional Energy Balance Equation [*Lovejoy*, 2021a; b]
950 (FEBE). The FEBE can also be derived phenomenologically by assuming that energy
951 storage processes are scaling, [*Lovejoy*, 2019a; 2019b; *Lovejoy et al.*, 2021]).
952   When forced by a Gaussian white noise, the FEBE is also a generalization of
953 fractional Gaussian noise (fGn) and its integral (fractional Relaxation motion, fRm),
954 generalizes fractional Brownian motion (fBm). More classically, it generalizes the
955 Orenstein-Uhlenbeck process that corresponds to the $h =1$ special case (i.e. the standard
956 EBE with white noise forcing). Over the parameter range $0 < h < 1/2$, the high frequency
957 FEBE limit (fGn) has been used as the basis of monthly and seasonal temperature forecasts
958 [*Lovejoy et al.*, 2015], [*Del Rio Amador and Lovejoy*, 2019; *Del Rio Amador and Lovejoy*,
959 2021a; *Del Rio Amador and Lovejoy*, 2021b]; at one month lead times, these macroweather
960 forecasts are similar in skill to conventional numerical models whereas for bimonthly,
961 seasonal and annual forecasts they are more skillful [*Del Rio Amador and Lovejoy*, 2021a].
962 For multidecadal time scales the low frequency limit has been used as the basis of climate
963 projections through to the year 2100 [*Hebert*, 2017], [*Lovejoy et al.*, 2017], [*Hébert et al.*,
964 2021], and more recently, the full FEBE has been used directly [*Procyk et al.*, 2020],
965 [*Procyk*, 2021].
966   It was the success of predictions and projections with different exponents but
967 theoretically derived the same empirical underlying FEBE $h \approx 0.4$, that over the last years,
968 motivated the development of the FEBE (announced in [*Lovejoy*, 2019a]) and the work
969 reported here. The statistical characterizations – correlations, structure functions, Haar
970 fluctuations and spectra as well as the predictability properties are important for these and
971 other FEBE applications and are derived in this paper.
972   While the deterministic fractional relaxation equation is classical, various technical
973 difficulties arise when it is generalized to the stochastic case: in the physics literature, it is
974 a Fractional Langevin Equation (FLE) that has almost exclusively been considered as a
975 model of diffusion of particles starting at an origin. This requires $t = 0$ initial conditions
976 that imply that the solutions are strongly nonstationary. In comparison, the Earth's
977 temperature fluctuations that are associated with its internal variability are statistically
978 stationary. This can easily be modelled with initial conditions at $t = -\infty$ i.e. by using Weyl
979 fractional derivatives. In addition, in the usual FLE, the highest order derivative is an
980 integer so that sample processes are RMS differentiable order at least one ([*Watkins et al.*,

981 2020] have called the FEBE a "Fractionally Integrated FLE") . In the FEBE and the
982 fractionally integrated extensions, the highest order derivative is readily of order <1/2 so
983 that sample processes are generalized functions ("noises") and must be smoothed/averaged
984 for physical applications.
985   Although EBE's were originally developed to understand the deterministic
986 temperature response to external forcing, the temperature also responds to stochastic
987 "internal" forcing. While the Earth system variability is generally highly nonGaussian
988 (multifractal, [*Lovejoy*, 2018]), the temporal macroweather regime modelled here is the
989 quasi-Gaussian exception. This paper therefore explores the statistics of the temperature
990 response when it is stochastically forced by Gaussian processes: both by white noise ($\alpha =$
991 0) and by a (long memory) fractional Gaussian noise (fGn) processes. The white noise
992 special case –"pure fRn, fRm" - is the $\alpha = 0$ special case, fGn forced case extends the
993 parameter range to $0 \le \alpha < 1/2$. According to work in progress using satellite and reanalysis
994 radiances, both cases appear to be empirically relevant for modelling the Earth's energy
995 balance.
996   A key novelty is therefore to consider the fractional relaxation - equation (a
997 Fractional Langevin Equation, FLE) forced by white and scaling noises starting from
998 $t = -\infty$: equivalent to Weyl "fractionally integrated fractional relaxation equation"). In
999 addition, the highest order terms in standard FLE's are integer ordered, the fractional terms
1000 represent damping and are of lower order, guaranteeing that solutions are regular functions.
1001 However, the FEBE's highest order term is fractional and over the main empirically
1002 significant parameter range ($\alpha+h<1/2$) the processes are noises (generalized functions): in
1003 order to represent physical processes, they must be averaged. This is conveniently handled
1004 by introducing their integrals or "motions". We proceeded to derive their fundamental
1005 statistical properties including series expansions about the origin and infinity. These
1006 expansions are nontrivial since they mix fractional and integer ordered terms (Appendix
1007 A). Since the FEBE is used as the basis for macroweather predictions, the theoretical
1008 predictability skill is important in applications and was also derived.
1009   With these stationary Gaussian forcings, the solutions are a new stationary process
1010 – fractional Relaxation noise (fRn, $\alpha =0$) and their extensions to fractionally integrated fRn
1011 processes ($\alpha>0$). Over the range $0 < \alpha + h < 1/2$, we show that the small scale limit is a
1012 fractional Gaussian noise (fGn) – and its integral - fractional Relaxation motion (fRm) -
1013 has stationary increments and which generalizes fractional Brownian motion (fBm).
1014 Although at long enough times, the fRn ($\alpha = 0$) tends to a Gaussian white noise, and fRm
1015 to a standard Brownian motion, this long time convergence is typically very slow (when
1016 $\alpha>0$, the long time behaviours are fGn and fBm processes, parameter α).
1017   Much of the effort was to deduce the asymptotic small and large scale behaviours
1018 of the autocorrelation functions that determine the statistics and in verifying these with
1019 extensive numerical simulations. An interesting exception was the $h = 1/2$ special case
1020 which for fGn corresponds to an exactly 1/f noise. Here, we give the exact mathematical
1021 expressions for the full correlation functions, showing that they had logarithmic
1022 dependencies at both small and large scales. The resulting Half order EBE (HEBE) has an
1023 exceptionally slow transition from small to large scales (a factor of a million or more is
1024 needed) and empirically, it is quite close to the global temperature series over scales of
1025 months, decades and possibly longer.

Beyond improved monthly, seasonal temperature forecasts and multidecadal projections, the stochastic FEBE opens up several paths for future research. One of the more promising is to apply these techniques to the spatial FEBE and generalize it in various directions. This is a follow up on the special value $h = 1/2$ that is very close to that found empirically and that can be analytically deduced from the classical Budyko-Sellers energy transport equation by improving the mathematical treatment of the radiative boundary conditions [*Lovejoy*, 2021a; b]. In the latter case, one obtains a partial fractional differential equation for the horizontal space-time variability of temperature anomalies over the Earth's surface, allowing regional forecasts and projections. This has already allowed improved regional projections ([*Procyk*, 2021]) and promises better monthly, seasonal forecasts.

While the FEBE has already demonstrated its ability to project future climates, these improvements will allow for the modelling of the nonlinear albedo-temperature feedbacks needed for modelling of transitions between different past climates. Finally, the FEBE is a promising candidate for a high level stochastic model that accounts for the collective interactions of huge numbers of degrees of freedom [*Lovejoy*, 2019a]. In comparison, conventional GCM approaches attempt to explicitly model as many degrees of freedom as possible. If they achieve their aim of making climate projections from "cloud resolving" GCMs, they will model structures that live for only 15 minutes and then–average them over decades.

Acknowledgements

Appendix A: The small and large scale fRn, fRm statistics:

A.1 $R_{\alpha,h}(t)$ as a Laplace transform

In section 2.4, we derived general statistical formulae for the auto-correlation functions of motions and noises defined in terms of Green's functions of fractional operators. Since the processes are Gaussian, autocorrelations fully determine the statistics. While the autocorrelations of fBm and fGn are well known those for fRm and fRn are new and are not so easy to deal with since they involve quadratic integrals of Mittag-Leffler functions. In this appendix, we derive the basic power law expansions as well as large t (asymptotic) expansions, and we numerically investigate their accuracy.

It is simplest to start with the Fourier expression for the autocorrelation function for the unit white noise forcing (eq. 33). First convert the inverse Fourier transform (eq. 66) into a Laplace transform. For this, consider the integral over the contour C in the complex plane:

$$I(z) = \frac{1}{2\pi} \int_C \frac{e^{zt}}{z^\alpha (-z)^\alpha (1+z^h)(1+(-z)^h)} dz \qquad \text{(A.1)}$$

Take C to be the closed contour obtained by integrating along the imaginary axis (this part gives $R_{\alpha,h}(t)$, eq. 33), and closing the contour along an (infinite) semicircle over the second and third quadrants. When $0<h<1$, there are no poles in these quadrants, but we must integrate around a branch cut on the negative real axis. When $1<h<2$, we must take into account two new branch cuts and two new poles in the -ve real plane. In a polar representation $z = re^{i\theta}$, the additional branch cuts are along the rays $z = re^{\pm i\pi/h}$; $r>1$, circling around the poles at $z = e^{\pm i\pi/h}$. The additional branch cuts give no net contribution, but the residues of the poles do make a contribution ($P_{\alpha,h} \neq 0$ below). We can express both cases with the formula:

$$R_{\alpha,h}(t) = -\frac{1}{\pi} \operatorname{Im} \int_0^\infty \frac{e^{-xt} dx}{x^{2\alpha} e^{i\alpha\pi}(1+x^h)(1+x^h e^{i\pi h})} + P_{\alpha,h,+}(t); \quad t>0$$

$$\text{(A.2)}$$

"Im" indicates the imaginary part and:

$$P_{\alpha,h,\pm}(t) = 0; \qquad\qquad 0<h<1$$

$$P_{\alpha,h,\pm}(t) = -e^{t\cos\left(\frac{\pi}{h}\right)} \frac{\sin\left(\pm\frac{\pi}{h}(1-\alpha) + \frac{h\pi}{2} + t\sin\left(\frac{\pi}{h}\right)\right)}{h\sin\left(\frac{\pi h}{2}\right)}; \quad 1<h<2 \qquad 0 \le \alpha < 1/2$$

$$\text{(A.3)}$$

1078 While the integral term is monotonic, the $P_{\alpha,h}$ term oscillates with frequency
1079 $\omega = 2\pi / \sin(\pi/h)$. $P_{\alpha,h}$ accounts for the oscillations visible in figs. 2, 3, 5b although since
1080 when $1<h<2$, $\cos(\pi/h)<1$, they decay exponentially. When $h>1$, this pole contribution
1081 dominates $R_{\alpha,h}(t)$ for a wide range of t values around $t = 1$, although as we see below,
1082 eventually at large t, power law terms come to the fore.
1083
1084 Comments:
1085 a) When $\alpha = 0$, $h = 1$, we obtain the classical Ornstein-Uhlenbeck autocorrelation:

1086 $$R_{0,1}(t) = \frac{1}{2}e^{-|t|}.$$

1087 b) In the case $h = 0$, the process reduces to an fGn process:
1088 $R_{\alpha,0}(t) = t^{-1+2\alpha}\Gamma(1-2\alpha)\sin(\pi\alpha)/(4\pi)$. There is an extra factor of 4 that comes from the
1089 small h limit $_{-\infty}D_t^h + 1 \to 2$.

1090 **A.2 Asymptotic expansions:**
1091   An advantage of writing $R_{\alpha,h}(t)$ as a Laplace transform is that we can use Watson's
1092 lemma to obtain an asymptotic expansion (e.g. [*Bender and Orszag*, 1978]). The idea is
1093 that an expansion of eq. A.2 around $x = 0$ can be Laplace transformed term by term to yield
1094 an asymptotic expansion for large t.
1095   The expansion of the integrand around $x = 0$ can be obtained from a binomial
1096 expansion (see also A.10):

$$\frac{1}{x^{2\alpha}e^{i\pi\alpha}(1+x^h)(1+x^he^{i\pi h})} = \frac{e^{-i\pi\alpha}}{e^{i\pi h}-1}\sum_{n=0}^{\infty}(-1)^n\left(e^{i(n+1)\pi h}-1\right)x^{-2\alpha+nh}; \quad x<1$$

1097
1098   (A.4)
1099 this leads to:

1100 $$-\frac{1}{\pi}\,\mathrm{Im}\,\frac{1}{x^{2\alpha}e^{i\alpha\pi}(1+x^h)(1+x^he^{hi\pi})} = -\sum_{n=0}^{\infty}D_{-n}x^{nh-2\alpha} \qquad \text{(A.5)}$$

1101 $$D_n = (-1)^{n+1}\frac{\cos\left(\left(n-\frac{1}{2}\right)\pi h + \alpha\pi\right) - \cos\left(\frac{\pi h}{2}+\alpha\pi\right)}{2\pi\sin\left(\frac{\pi h}{2}\right)} = (-1)^n\frac{\sin\left(\frac{n\pi h}{2}+\alpha\pi\right)\sin\left(\frac{(n-1)\pi h}{2}\right)}{\pi\sin\left(\frac{\pi h}{2}\right)}$$

1102 (note D_{-n} is used in the expansion here; D_n is used below).
1103   Therefore, taking the term by term Laplace transform and using Watson's lemma:

1104 $$R_{\alpha,h}(t) = -\sum_{n=0}^{\infty}D_{-n}\Gamma(1+nh-2\alpha)t^{2\alpha-(1+nh)} + P_{\alpha,h,+}(t); \qquad t \gg 1$$

1105 $(0<\alpha<1/2)$ (A.6)
1106 Where we have included the exponentially decaying residue $P_{\alpha,h,+}$ that contributes when
1107 $1<h<2$. Note that although Γ diverges for all negative integer arguments, using the identity

1108 $\quad\Gamma(1+hn-2\alpha)\sin((nh-2\alpha)\pi)=-\pi/\Gamma(2\alpha-nh)\qquad$ we $\quad$ see $\quad$ that $\quad$ the $\quad$ product

1109 $\quad\sin((nh-2\alpha)\pi)\Gamma(2\alpha-nh)$ is finite.

1110 $\qquad$ The first terms are explicitly:

1111
$$R_{\alpha,h}(t)=\frac{\Gamma(1-2\alpha)\sin(\pi\alpha)}{\pi}t^{2\alpha-1}-\frac{\cos\left(\dfrac{\pi h}{2}\right)}{\cos\left(\dfrac{\pi h}{2}-\pi\alpha\right)\Gamma(2\alpha-h)}t^{2\alpha-(1+h)}+...$$

1112 $\hfill t\gg 1\qquad\qquad$ (A.7)

1113 We see that when $\alpha\neq0$, $D_0>0$ so that as expected, the leading behaviour has no h

1114 dependence, it is only due to the long range correlations in the forcing; we obtain the fGn

1115 result: $t^{2\alpha-1}$. However for the pure fRn case, $\alpha=0$ and $D_0=0$ and we obtain:

1116
$$R_{0,h}(t)=\sum_{n=1}^{\infty}(-1)^{n}\frac{1+\cot\left(\dfrac{\pi h}{2}\right)\tan\left(\dfrac{n\pi h}{2}\right)}{2\Gamma(-nh)}t^{-(1+nh)}+P_{0,h,+}(t);\quad t\gg1\qquad\text{(A.8)}$$

1117 i.e. with leading behaviour is $t^{-(1+h)}$. Note that the leading $n=1$ coefficient reduces to

1118 $-1/\Gamma(-h)$ and that for $0<h<1$, $\Gamma(-h)<0$.

1119 $\qquad$ For the motions (fRm), we need the expansion of $V_{\alpha,h}(t)$, it can be obtained by

1120 integrating $R_{\alpha,h}$ twice (using eq. 36):

1121
$$V_{\alpha,h}(t)=a_{\alpha,h}t+b_{\alpha,h}-2\sum_{n=0}^{\infty}D_{-n}\Gamma(-1+nh-2\alpha)t^{2\alpha+1-nh}+2P_{\alpha,h,-}(t);\quad t\gg1\qquad 0\le\alpha<1/2$$

1122 $\hfill$ (A.9)

1123 Where $P_{\alpha,h-}$ is from the poles when $1<h<2$. Since the asymptotic expansion is not valid for

1124 $t=0$, we used the indefinite integrals of $R_{\alpha,h}$ hence there is a linear $a_{\alpha,h}t+b_{\alpha,h}$ term from

1125 the constants of integration. However, when $\alpha>0$, the leading term is the $t^{2\alpha+1}$ term from

1126 the fGn forcing and in the pure fRn case ($\alpha=0$), we can take $\lim_{\alpha\to0}\left(-2D_0\Gamma(-1-2\alpha)t^{2\alpha+1}\right)=t$

1127 so that the leading term $n=0$ already gives the correct fRm behaviour: $V_{\alpha,h}(t)\approx t$ so that

1128 $a_{0,h}=0$ ($b_{0,h}$ can be determined numerically).

1129

1130 **A.3 Power series expansions about the origin:**

1131 $\qquad$ For many applications one is interested in the behavior of $R_{\alpha,h}(t)$ for scales of

1132 months which is typically less than the relaxation time, i.e. $t<1$. It is therefore important

1133 to understand the small t behaviour. We again consider the Laplace integral for the $0<h<1$

1134 case. In this case, we can divide the range of integration in eq. A2 into two parts for $0<x<1$

1135 and $x>1$. For the former, we use the expansion in eq. A4 and for the latter:

1136
$$\frac{1}{x^{2\alpha}e^{i\pi\alpha}\left(1+x^{h}\right)\left(1+x^{h}e^{i\pi h}\right)}=\frac{e^{-i\pi\alpha}}{e^{i\pi h}-1}\sum_{n=1}^{\infty}(-1)^{n+1}\left(e^{-i(n-1)\pi h}-1\right)x^{-2\alpha-nh};\quad x>1\quad\text{(A.10)}$$

1137

1138 We can now integrate each term seperately using:

$$\int_0^1 e^{-xt} x^{nh-2\alpha}\, dx = \sum_{j=1}^{\infty} \frac{(-1)^{j-1}}{(hn-2\alpha+j)\Gamma(j)} t^{j-1}$$

1139

$$\int_1^{\infty} e^{-xt} x^{-(nh+2\alpha)}\, dx = E_{nh+2\alpha}(t) = \pi \frac{t^{-1+hn+2\alpha}}{\sin(\pi nh+2\pi\alpha)\Gamma(hn+2\alpha)} + \sum_{j=1}^{\infty} \frac{(-1)^{j-1}}{(hn+2\alpha-j)\Gamma(j)} t^{j-1}$$

1140 (A.11)

1141 where $E_\beta(t) = \int_1^{\infty} e^{-xt} x^{-\beta}\, dx$ is the exponential integral. Adding the two integrals and

1142 summing over n, we obtain:

1143 $$R_{\alpha,h}(t) = \sum_{n=2}^{\infty} D_n \Gamma(1-hn-2\alpha) t^{-1+hn+2\alpha} + \sum_{j=1}^{\infty} F_j \frac{t^{j-1}}{\Gamma(j)} \qquad\text{(A.12)}$$

1144 $$F_j = \frac{1}{\pi h}\,\text{Im}\!\left[\frac{e^{-i\alpha\pi}}{e^{i\pi h}-1}\!\left(e^{i\pi h}\sum_{n=-\infty}^{\infty}(-1)^n \frac{e^{i\pi nh}}{(n+a)} - \sum_{n=-\infty}^{\infty}(-1)^n \frac{1}{(n+a)}\right)\right]; \quad a = \frac{j-2\alpha}{h}$$

1145

1146 (we have interchanged the order of summations and used D_n from eq. A5 with $n>0$).

1147   The series for the coefficient F_j can now be summed analytically. Although the

1148 sum is a special case of the Lipchitz summation and Poisson summation formulae, the

1149 easiest method is to use the Sommerfeld-Watson transformation (e.g. [*Mathews and*

1150 *Walker*, 1973]) that converts an infinite sum into a contour integral that is then deformed.

1151 The Sommerfeld-Watson transformation states that for a an analytic function $f(z)$ that goes

1152 to zero at least as fast as $|z|^{-1}$, that:

1153 $$\sum_{n=-\infty}^{\infty}(-1)^n f(n) = -\pi \sum_k \frac{R_k}{\sin \pi z_k} \qquad\text{(A.13)}$$

1154 Where z_k is the location of the poles of $f(z)$ and R_k is the residue of the corresponding pole.

1155 In the above, take:

$$f(z) = \frac{e^{iz\pi h}}{(z+a)}$$

1156 (A.14)

1157 There is a single pole at $z_1 = -a$ and the residue is $R_1 = e^{-ia\pi h}$, therefore:

$$e^{i\pi h}\sum_{n=-\infty}^{\infty} \frac{(-1)^n e^{in\pi h}}{(n+a)} = \pi \frac{e^{i\pi h(1-a)}}{\sin \pi a}$$

1158 (A.15)

1159   The second sum needed in F_j can be obtained using $h = 0$ in the above so that

1160 overall:

1161

1162 $$F_j = \frac{1}{h\pi} \text{Im}\left[\frac{e^{-i\alpha\pi}}{e^{i\pi h}-1}\left(\pi\frac{e^{i\pi h(1-a)}-1}{\sin\pi a}\right)\right] = \frac{1}{h\sin\left(\pi(j-2\alpha)/h\right)}\text{Im}\left[\frac{e^{-i\pi j}e^{i\pi(h/2+\alpha)}-e^{-i\pi(h/2+\alpha)}}{e^{i\pi h/2}-e^{-i\pi h/2}}\right]$$
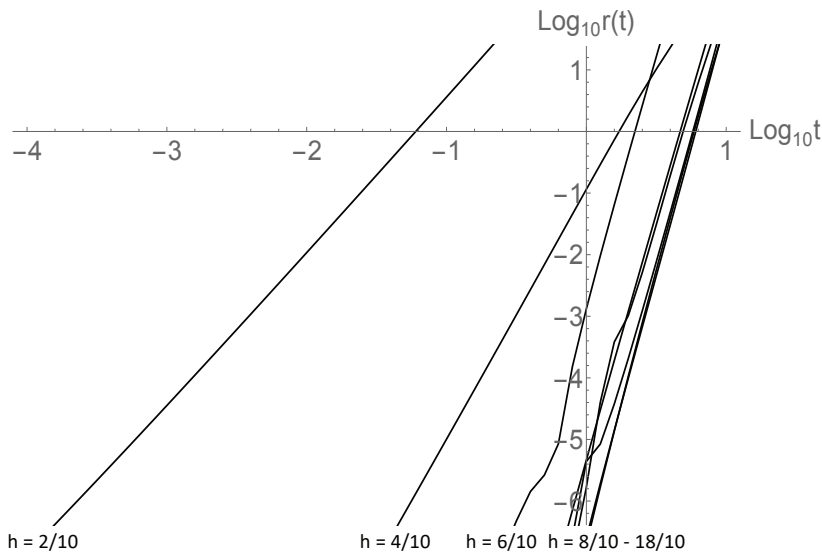
1163 $$\text{(A.16)}$$

1164 If j is even, then the term in the square bracket is pure real hence F_j vanishes.
1165 Otherwise:

$$F_j = -\frac{\cos\pi\left(\dfrac{h}{2}+\alpha\right)}{h\sin\left(\dfrac{\pi h}{2}\right)\sin\left(\dfrac{\pi}{h}(j-2\alpha)\right)}$$

1166 $$\text{(A.17)}$$

1167
1168 Note that $F_1>0$ for $h + \alpha > 1/2$ (with $0\le\alpha<1/2$, $0\le h<2$), whereas for $h + \alpha < 1/2$ it is quite
1169 complicated (see below).

1170
1171 Fig. A1: This shows the logarithm of the relative error in the $R_{0,h}^{(10,10)}(t)$ approximation (i.e.
1172 with 10 fractional terms and 10 integer order terms) with respect to the deviation from the fGn
1173 $R_{0,h}(t)$ $r = \log_{10}\left|1-\left(R_h^{fGn}(t)-R_{0,h}^{(10,10)}(t)\right)/\left(R_h^{fGn}(t)-R_{0,h}(t)\right)\right|$. The lines are for $h = 2/10$,
1174 $4/10,\dots,16/10, 18/10$ (excluding the exponential case $h = 1$), from left to right (note convergence
1175 is only for irrational h, therefore an extra 10^{-4} was added to each h). For the low h values the
1176 convergence is particularly slow.

1177

1178 Comments:

1179   1) These and the following formulae are for $t>0$; in addition, only the even integer
1180 ordered terms are non zero (the sum over odd j).

1181   2) Each integer term of the expansion F_j is itself obtained as an infinite sum, so that
1182 the overall result for $R_{\alpha,h}(t)$ is effectively a doubly infinite sum. This procedure swaps the
1183 order of the summation and apparently explains the fact that while the expansions were
1184 derived for the case $0<h<1$, the final expansion is valid for $0\leq\alpha<1/2$ and the full range
1185 $0<h<2$: numerically, it accurately reproduces the oscillations when $h>1$.

1186   3) The fGn correlation function is given by the single $n=2$ term:

1187
$$R_h^{(fGn)}(t) = D_2\Gamma(1-2h)t^{-1+2h} = \frac{\sin(h\pi)}{\pi}\Gamma(1-2h)t^{-1+2h} \qquad (A.18)$$

1188 It is also proportional to the correlation function of the fGn forced $h=0$, fRn process:

1189
$$R_h^{(fGn)}(t) = 4R_{\alpha=h,0}(t).$$

1190   4) When $0<\alpha+h<1/2$, R is divergent at the origin; this leading term
1191 $\Gamma(-1-2(h+\alpha))\sin(\pi(h+\alpha))t^{-1+2(h+\alpha)}/\pi$ is only dependent on $h+\alpha$ corresponding to an

1192 fGn with parameter $h+\alpha$. When $\frac{1}{2}<h+\alpha<2$, it is still the leading term fractional term, but
1193 the constant F_1 dominates at small t.

1194   5) The F_j terms diverge when $(j-2\alpha)/h$ is an integer. For example, if $\alpha=0$, the
1195 overall sum over all j thus diverges for all rational h. For irrational h, the convergence
1196 properties are not easy to establish, although due to the Γ functions, these series apparently
1197 converge for all $t\geq 0$, but the convergence is rather slow.

1198   Fig. A1 shows some numerical results for $\alpha=0$ showing the convergence of the
1199 10th order fractional 10th order integer power approximation ($n_{max}=j_{max}=10$). Since the
1200 leading (fGn) term diverges for small t, when $h\leq 1/2$ it is more useful to consider the
1201 convergence of the difference with respect to the fGn term i.e. $R_h^{(fGn)}(t)-R_{0,h,a}(t)$ where
1202 the approximation $R_{0,h,a}(t)$ is from the sum from $n=3$ to 10 and odd $j\leq 9$. Fig. A1 shows
1203 the logarithm of the ratio of the approximation with respect to the true value:
1204 $r=\log_{10}\left|1-\left(R_h^{(fGn)}(t)-R_{0,h,a}(t)\right)/\left(R_h^{(fGn)}(t)-R_{0,h}(t)\right)\right|$ (to avoid exact rationals, 10^{-4} was
1205 added to the h values). From the figure we see that the approximation is satisfactory except
1206 for small h. In the next section we return to this.

1207   6) For $\alpha+h>1/2$, when $t=0$, the only nonzero term is from the constant F_1: $R_{\alpha,h}(0)$
1208 $=F_1$, this gives the normalization constant. Comparing with eq. 27, we therefore have:

1209
$$R_{\alpha,h}(0) = \int_0^\infty G_{\alpha,h}(u)^2\,du = F_1 = -\frac{\cos\pi\left(\frac{h}{2}+\alpha\right)}{h\sin\left(\frac{\pi h}{2}\right)\sin\left(\frac{\pi}{h}(1-2\alpha)\right)}; \quad \alpha+h>1/2; \quad \begin{matrix}0\leq\alpha<1/2\\ 1/2<h<2\end{matrix}$$

1210   (A.19)

1211 Similarly, when $\alpha+h > 3/2$, for the quadratic the squared integral of $G'_{\alpha,h}$ is finite and it
1212 gives the coefficient of the t^2 term so that:

$$\int_0^\infty G'_{\alpha,h}(s)^2 \, ds = -\frac{F_3}{\Gamma(3)} = \frac{\cos\left(\frac{\pi}{2}(h+2\alpha)\right)}{2h\sin\left(\frac{\pi h}{2}\right)\sin\left(\frac{\pi}{h}(3-2\alpha)\right)}; \quad h+\alpha > \frac{3}{2}$$

1213   (A.20)

1214   7) The expression for $V_{\alpha,h}(t)$ can be obtained by integrating twice (eq. 36).
1215   8) In the special cases $h = 1/m$, with m a positive integer, F_j is independent of j and
1216 the integer powered series can be summed yielding a result proportional to $\cosh t$. However,
1217 this large t divergence is cancelled out by the fractional term and the result is finite (this
1218 partial cancellation is discussed in the next subsection). The special important case $h = 1/2$
1219 is dealt with in appendix B.

A.4 A Convenient approximation
1220
1221   The expansion for $R_{\alpha,h}$ is the sum of a fractional and an integer ordered series.
1222 Partial sums appear to converge (fig. A1), albeit slowly. For simplicity, we consider the
1223 case of primary interest, a pure fRn process ($\alpha = 0$). Examination of partial sums shows
1224 that the integer ordered and fractional ordered terms tend to cancel, the difficulty due to
1225 the coefficient of the integer ordered terms $j \approx hn + 2\alpha$ that includes that comes from the
1226 exponential integral and can large when $j \approx hn + 2\alpha$. This suggests an alternative way of
1227 expressing the series:

1228
$$R_{0,h}(t) = \sum_{n=2}^{\infty} D_n E_{nh}(t) + \sum_{j=1}^{\infty} C_j \frac{(-1)^{j-1}}{\Gamma(j)} t^{j-1}; \quad C_j = \sum_{n=2}^{\infty} \frac{D_n}{(hn+j)} \qquad \text{(A.21)}$$

1229
1230 Where D_n is given by eq. A.5 and the n sums start at $n = 2$ since $D_1 = 0$. C_j can be expressed
1231 as:

1232
$$C_j = -\frac{ie^{-ih\pi}}{2\pi h(e^{ih\pi}-1)}\left(-\left(e^{ih\pi}+e^{2ih\pi}\right)\Phi\left(-1,1,1+\frac{j}{h}\right) + \Phi\left(e^{ih\pi},1,1+\frac{j}{h}\right) + e^{3ih\pi}\Phi\left(e^{-ih\pi},1,1+\frac{j}{h}\right)\right)$$

1233   (A.22)

1234 where Φ is the Hurwitz-Lerch phi function $\Phi(z,s,a) = \sum_{n=0}^{\infty} z^n (n+a)^{-s}$.

1235 We can also expand the exponential integral:

1236
$$E_{nh}(t) = \pi\frac{t^{-1+hn}}{\sin(\pi nh)\Gamma(hn)} + \sum_{j=1}^{\infty} \frac{(-1)^{j-1}}{(hn-j)\Gamma(j)} t^{j-1} \qquad \text{(A.23)}$$

1237 For the j_{max} and n_{max} partial sums, we have:

1238
$$R_{h,n_{max},j_{max}}(t) = \sum_{n=2}^{n_{max}} D_n \Gamma(1-nh)t^{-1+hn} + \sum_{j=1}^{j_{max}} F_{j,n_{max}} \frac{(-1)^{j-1}}{\Gamma(j)} t^{j-1}; \quad F_{j,n_{max}} = C_j + \sum_{n=2}^{n_{max}} \frac{D_n}{hn-j}$$

1239   (A.24)

1240 Now define the (j_{max}, n_{max}) approximation by:

1241
$$R_{0,h,n_{max},j_{max}}(t) = \frac{R_{0,h}^{(n_{max}+1,j_{max})}(t) + R_{0,h}^{(n_{max},j_{max})}(t)}{2} \qquad (A.25)$$

1242 This has the effect of adding in half the next higher n term and is more accurate; overall,
1243 j_{max} and n_{max} may now be taken to be much smaller than in the previous approximation. For
1244 example putting $n_{max} = 2, j_{max} = 1$, we get with the partial sum:

1245
$$R_{0,h,2,1}(t) = R_h^{(fGn)}(t) + \frac{D_3}{2}\Gamma(1-3h)t^{-1+3h} + F_1 \qquad (A.26)$$

1246 Where:

1247
$$F_1 = C_1 + \frac{D_2}{2h-1} + \frac{D_3}{2(3h-1)}$$

$$D_2 = \frac{\sin(\pi h)}{\pi}; \quad D_3 = -\frac{\sin(\pi h)(1+2\cos(\pi h))}{\pi}$$

1248 $\qquad (A.27)$
1249   To understand the behaviour, fig. A2 shows the behaviour of coefficient of the

1250 t^{1+3h} term $\frac{D_3}{2}\Gamma(1-3h)$, the constant term F_1 and the coefficient of the next integer (linear

1251 in t) term $F_2 = C_2 + \frac{D_2}{2h-2} + \frac{D_3}{2(3h-2)}$. Up until the end of the fGn region ($h = 1/2$), the

1252 t^{1+3h} and F_1 terms have opposite signs and tend to cancel. In addition, we see that for t
1253 $\approx<1$ and $h<1$, they dominate over the (omitted) linear term. Fig. A3 shows that the $R_{0,h,2,1}$
1254 approximation is surprisingly good for $h<1$ and is still not so bad for $1< h <2$. This
1255 approximation is thus useful for monthly resolution macroweather temperature fields that
1256 have relaxation times of years or longer and where h is mostly over the range $0< h <1/2$,
1257 but over some tropical ocean regions can increase to as much as $h \approx 1.2$ ([*Del Rio Amador*
1258 *and Lovejoy*, 2021a]). Fig. A3 shows that the (2,1) approximation is reasonably accurate
1259 for $t \approx<1$, especially for $h<1$.
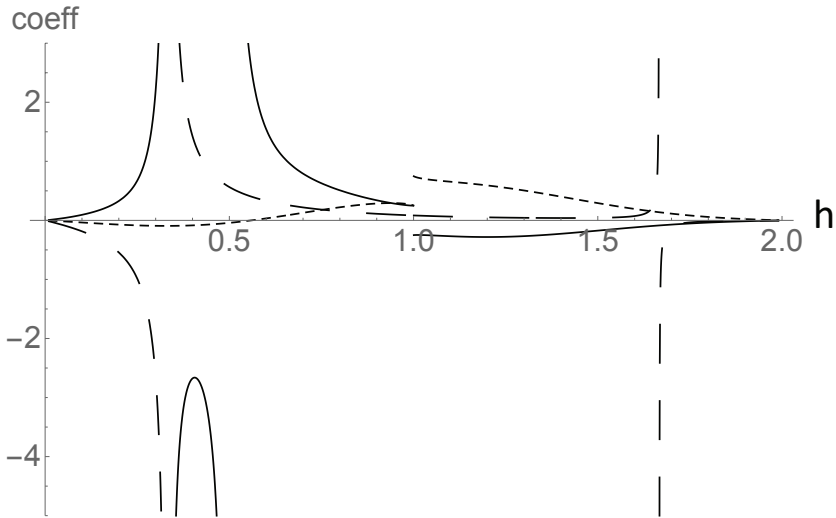
Fig. A2: The solid line is the constant term F_1, the long dashes are the coefficients $\frac{D_3}{2}\Gamma(1-3h)$ of the fractional power, the short dashes are the coefficients of the linear term: $F_2 = C_2 + \frac{D_2}{2h-2} + \frac{D_3}{2(3h-2)}$. We can see that the contribution of the linear term (used in the $R_{0,h,2,2}(t)$ approximation) for $h<1$ and $t<1$ is fairly small; whereas for $1<h<2$, it is larger and the $R_{0,h,2,2}(t)$ approximation is significantly better than the $R_{0,h,2,1}(t)$ approximation (see fig. A3).
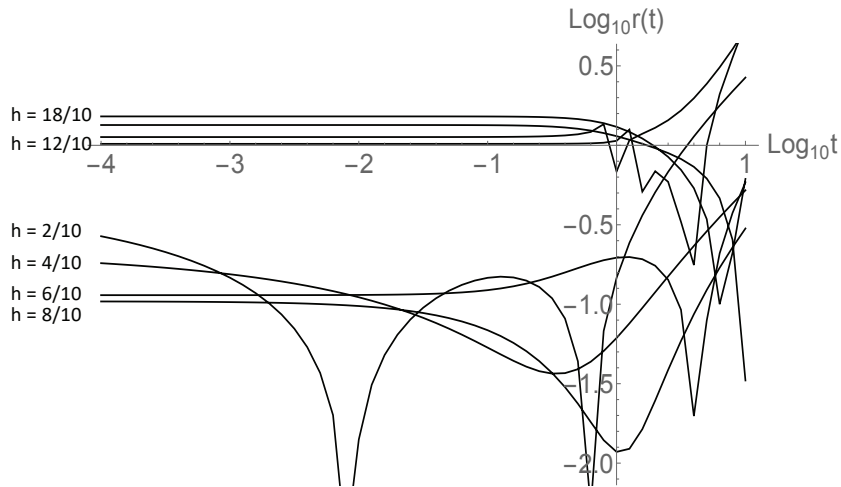
Fig. A3: This shows the logarithm of the relative error in the (2,1) approximation with respect to the deviation from the fGn $R_h(t)$ ($r = \log_{10}\left|1 - \left(R_h^{fGn}(t) - R_{0,h,2,1}(t)\right)/\left(R_h^{fGn}(t) - R_{0,h}(t)\right)\right|$). For $h<1$, $t<0$ it is of the order $\approx 30\%$ whereas for $h>1$, it of the order 100%. The $h = 1$ (exponential) curve is not shown although when $t<0$ the error is of order 60%.

1272

Appendix B: The h=1/2 special case

1274   When $\alpha = 0$, $h = 1/2$, the high frequency fGn limit is an exact "1/f noise", (spectrum
1275 ω^{-1}) it has both high and low frequency divergences. The high frequency divergence can
1276   be tamed by averaging, but not the low frequency divergence, so that fGn is only defined
1277   for $h<1/2$. However, for fRn, the low frequencies are convergent over the whole range 0
1278 $< h < 2$, and for $h = 1/2$ we find that the correlation function has a logarithmic dependence
1279   at both small and large scales. This is associated with particularly slow transitions from
1280   high to low frequency behaviours. The critical value $h = 1/2$ corresponds to the HEBE that
1281   was recently proposed [*Lovejoy*, 2021a; b] where it was shown that the value $h = 1/2$ could
1282   be derived analytically from the classical Budyko-Sellers energy balance equation.
1283   Therefore, $R_{\alpha,1/2}(t)$, $V_{\alpha,1/2}(t)$, characterize the statistics of the temperature response of the
1284   classical heat equation response to fGn forcing order α.
1285   It is possible to obtain exact analytic expressions for $R_{\alpha,1/2}(t)$, $V_{\alpha,1/2}(t)$ and the Haar
1286   fluctuations; we develop these in this appendix, for some early results, see [*Mainardi and*
1287   *Pironi*, 1996].
1288
1289   The starting point is the Laplace expression A2 with $h = 1/2$:

$$R_{\alpha,h}(t) = -\frac{1}{\pi} \operatorname{Im} e^{-i\alpha\pi} \int_0^\infty \frac{e^{-xt}dx}{x^{2\alpha}\left(1+x^{1/2}\right)\left(1+ix^{1/2}\right)} = -\frac{1}{\pi\sqrt{2}} \operatorname{Im} e^{-i\pi\alpha} \int_0^\infty x^{-2\alpha}\left(\frac{e^{i\pi/4}}{1+x^{1/2}} + \frac{e^{-i\pi/4}}{1+x} - \frac{e^{i\pi/4}x^{1/2}}{1+x} \right)e^{-xt}dx$$

(B1)

1291   We require the following Laplace transforms:

$$L_1(t) = \int_0^\infty \frac{e^{-xt}}{x^{2\alpha}\left(1+x^{1/2}\right)} dt = e^{-t-2i\pi\alpha}\left(\Gamma(1-2\alpha)\Gamma(2\alpha,-t) - i\Gamma\left(\frac{3}{2}-2\alpha\right)\Gamma\left(2\alpha-\frac{1}{2},-t\right) \right)$$

$$L_2(t) = \int_0^\infty \frac{e^{-xt}}{x^{2\alpha}\left(1+x\right)} dt = e^t\Gamma(1-2\alpha)\Gamma(2\alpha,t)$$

$$L_3(t) = \int_0^\infty \frac{e^{-xt}x^{1/2}}{x^{2\alpha}\left(1+x\right)} dt = e^t\Gamma\left(\frac{3}{2}-2\alpha\right)\Gamma\left(2\alpha-\frac{1}{2},t\right)$$

1292
1293   (B.2)

1294   Where we have introduced the incomplete gamma function: $\Gamma(a,z) = \int_z^\infty u^{a-1}e^{-u} du$ (with a

1295   branch cut in the complex plane from $-\infty$ to 0). The general result is thus:

1296 $$R_{\alpha,1/2}(t) = \frac{1}{2\pi}\left(\sin\pi\alpha\left(L_1(t)+L_2(t)-L_3(t)\right) + \cos\pi\alpha\left(-L_1(t)+L_2(t)+L_3(t)\right) \right)$$

1297   (B.3)

1298   Fig. B1 shows plots $R_{\alpha,1/2}(t)$ over 8 orders of magnitude in t, indicating the generally
1299 very slow converge to the asymptotic behaviour (shown as straight lines at the right).
1300   Fig. B1 also shows the singular small t behaviour of the pure fRn case ($\alpha = 0$). In
1301 this limit both L_1, and L_2, are singular - they both yield logarithmic small scale divergences.
1302 Pure fRn is of special interest, and yields the somewhat simpler result:

1303
$$R_{0,1/2}(t) = \frac{1}{2}\left(e^{-t}erfi\sqrt{t} - e^{t}erfc\sqrt{t}\right) - \frac{1}{2\pi}\left(e^{t}Ei(-t) + e^{-t}Ei(t)\right) ;$$

1304
$$Ei(z) = -\int_{-z}^{\infty} e^{-u}\frac{du}{u} ;$$

1305
$$erfi(z) = -i\left(erf(iz)\right); \quad erf(z) = \frac{2}{\sqrt{\pi}}\int_{0}^{z} e^{-s^2}\,ds \tag{B.4}$$

1306   We can use these results to obtain small and large t expansions:

1307
$$R_{0,1/2}(t) = -\left(\frac{2\gamma_E + \pi + 2\log t}{2\pi}\right) + \frac{2\sqrt{t}}{\sqrt{\pi}} - \frac{t}{2} - \left(\frac{3 + 2\gamma_E + \pi + 2\log t}{4\pi}\right)t^2 + O(t^{3/2}); \quad t \ll 1$$

1308 (B.5)

1309
$$R_{0,1/2}(t) = \frac{1}{2\sqrt{\pi}}t^{-3/2} - \frac{1}{\pi}t^{-2} + \frac{15}{8\sqrt{\pi}}t^{-7/2} + O(t^{-4}); \quad t \gg 1 ,$$

1310 where γ_E is Euler's constant $= 0.57...$ (the asymptotic formula can be obtained as a special
1311 case of eq. in appendix A, but note the logarithmic small scale divergence).

1312   To obtain the corresponding results for $V_{0,1/2}$ use: $V_{0,1/2}(t) = 2\int_{0}^{t}\left(\int_{0}^{v}R_{0,1/2}(u)\,du\right)dv$.
1313 The exact $V_{0,1/2}$ is:

1314
$$V_{0,1/2}(t) = G_{3,4}^{2,2}\left[t \middle| \begin{matrix} 2, & 2, & 5/2 \\ 2, & 2, & 0, & 5/2 \end{matrix}\right] + \frac{e^{t}}{\pi}\left(Shi(t) - Chi(t)\right) + \left(e^{-t}erfi\left(\sqrt{t}\right) - e^{t}erf\left(\sqrt{t}\right)\right)$$

$$+t\left(1 + \frac{\gamma_E - 1}{\pi}\right) - 4\sqrt{\frac{t}{\pi}} + \frac{(1+t)\log t}{\pi} + 1 + \frac{\gamma_E}{\pi}$$

1315 (B.6)
1316 where $G_{3,4}^{2,2}$ is the MeijrG function, Chi is the CoshIntegral function and Shi is the
1317 SinhIntegral function. The expansions are:

1318
$$V_{0,1/2}(t) = -\frac{t^2 \log t}{\pi} + \frac{191 - 156\gamma_E - 78\pi}{144\pi} + \frac{16}{15\sqrt{\pi}}t^{5/2} - \frac{t^3}{6} - \frac{t^4 \log t}{12\pi} + O(t^{3/2}); \quad t \ll 1$$

1319 (B.7)

1320
$$V_{0,1/2}(t) = t + \frac{\pi + 2\gamma_E}{\pi} + \frac{2\log t}{\pi} - \frac{4}{\sqrt{\pi}}t^{1/2} + \frac{1}{\sqrt{\pi}}t^{-1/2} - \frac{2}{\pi}t^{-2} + \frac{15}{4\sqrt{\pi}}t^{-3/2} + O(t^{-4}); \quad t \gg 1 .$$

1321   We can also work out the variance of the Haar fluctuations:

$$\left\langle \Delta U^2_{0,1/2}(\Delta t)_{Haar} \right\rangle = \frac{\Delta t^2 \log \Delta t}{4\pi} + \frac{6\pi + 12\gamma_E - \log 16 + 960 \log 2}{240\pi} + \frac{512(\sqrt{2}-2)}{240\sqrt{\pi}} \Delta t^{1/2} + \frac{\Delta t}{3} + O(\Delta t^{3/2}); \quad \Delta t \ll 1$$

$$(B.8)$$

$$\left\langle \Delta U^2_{0,1/2}(\Delta t)_{Haar} \right\rangle = 4\Delta t^{-1} - \frac{32\sqrt{2}}{\sqrt{\pi}} \Delta t^{-3/2} + \frac{3t^{-2} \log \Delta t}{\pi} + O(\Delta t^{-2}); \quad \Delta t \gg 1 \quad .$$

Figure B2 shows numerical results for $\alpha = 0$, $h = \frac{1}{2}$, the transition between small and large t behaviour is extremely slow; the 9 orders of magnitude depicted in the figure are barely enough. The extreme low $(R_{1/2})^{1/2}$ (dashed) asymptotes at the left to a slope zero (a square root logarithmic limit, eq. B8), and to a -3/4 slope at the right. The RMS Haar fluctuation (black) changes slope from 0 to -1/2 (left to right). Fig. B2 also shows the logarithmic derivative of the RMS Haar (black) compared to a regression estimate over two orders of magnitude in scale (dashed; a factor 10 smaller and 10 larger than the indicated scale was used, this represents a possible empirically accessible range). This figure underlines the gradualness of the transition from $h = 0$ to $h = -1/2$. If empirical data were available only over a factor of 100 in scale, depending on where this scale was with respect to the relaxation time scale (unity in the plot), the RMS Haar fluctuations could have any slope in the range 0 to -1/2 with only small deviations.
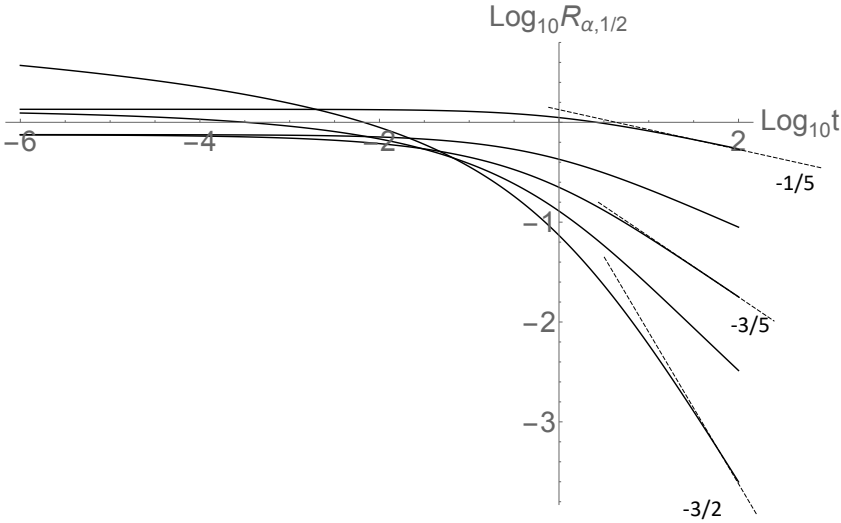
Fig. B1: $R_{\alpha,1/2}$ for α increasing from 0 (pure fRn) to 8/10 in steps of 1/10 (at right: bottom to top). The $\alpha = 0$ curve has a logarithmic divergence at small t (the far left). Recall from section

1341   that at large t, $R_{0,1/2} \approx t^{-3/2}$ and for $\alpha > 0$: $R_{\alpha,1/2} \approx t^{2\alpha-1}$, for $\alpha = 0, 1/5, 2/5$ the theoretical asymptotes of
1342   the leading terms are indicated for reference.
1343   .
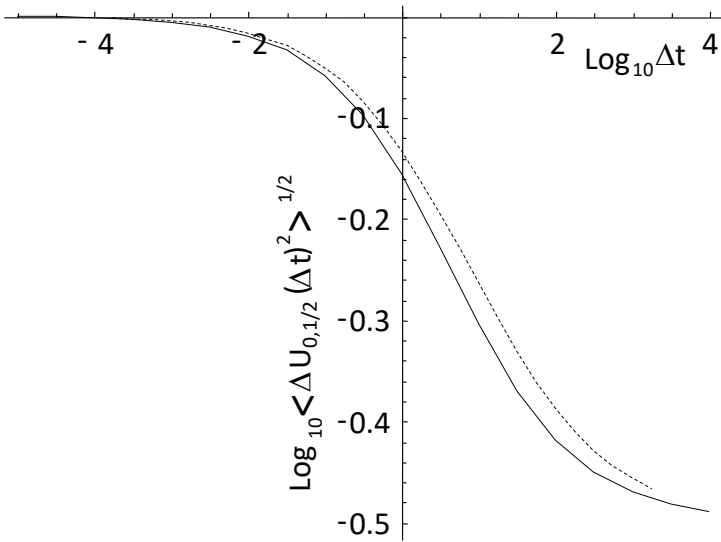
1344
1345   Fig. B2: The logarithmic derivative of the RMS Haar fluctuations of $U_{0,1/2}$ (solid) in fig.
1346   B1 compared to a regression estimate over two orders of magnitude in scale (dashed; a factor 10
1347   smaller and 10 larger than the indicated scale was used). This plot underlines the gradualness of
1348   the transition from slopes 0 to -0.5 corresponding to *apparent h* = 0 to h = -1/2 scaling. Over range
1349   of 100 or so in scale there is approximate scaling but with exponents that depend on the range of
1350   scales covered by the data. If data were available only over a factor of 100 in scale, the RMS Haar
1351   fluctuations could have any slope in the fGn range 0 to   -1/2 with only small deviations.
1352

1353
1354
1355   **References:**
1356   Atanackovic, M., Pilipovic, S., Stankovic, B., and Zorica, D., *Fractional Calculus with*
1357   *applications in mechanics: variations and diffusion processes*, 313 pp., Wiley,
1358   2014.
1359   Babenko, Y. I., *Heat and Mass Transfer*, Khimiya: Leningrad (in Russian), 1986.
1360   Bender, C. M., and Orszag, S. A., *Advanced mathematical methods for scientists and*
1361   *engineers*, Mc Graw Hill, 1978.
1362   Biagini, F., Hu, Y., Øksendal, B., and Zhang, T., *Stochastic Calculus for Fractional*
1363   *Brownian Motion and Applications*, Springer-Verlag, 2008.
1364   Budyko, M. I., The effect of solar radiation variations on the climate of the earth, *Tellus*,
1365   *21*, 611-619, 1969.
1366   Buizza, R., Miller, M., and Palmer, T. N., Stochastic representation of model
1367   uncertainties in the ECMWF Ensemble Prediction System, *Q. J. Roy. Meteor. Soc.*,
1368   *125*, 2887–2908, 1999.
1369   Chekroun, M. D., Simonnet, E., and Ghil, M., Stochastic Climate Dynamics: Random
1370   Attractors and Time-dependent Invariant Measures *Physica D*, *240*, 1685-1700
1371   2010.
1372   Coffey, W. T., Kalmykov, Y. P., and Titov, S. V., Characteristic times of anomalous
1373   diffusion in a potential, in *Fractional Dynamics: Recent Advances*, edited by J.
1374   Klafter, S. Lim and R. Metzler, pp. 51-76, World Scientific, 2012.
1375   Del Rio Amador, L., and Lovejoy, S., Predicting the global temperature with the
1376   Stochastic Seasonal to Interannual Prediction System (StocSIPS) *Clim. Dyn.*, *53*,
1377   4373–4411 doi: org/10.1007/s00382-019-04791-4., 2019.
1378   Del Rio Amador, L., and Lovejoy, S., Using regional scaling for temperature forecasts
1379   with the Stochastic Seasonal to Interannual Prediction System (StocSIPS), *Clim.*
1380   *Dyn.* doi: 10.1007/s00382-021-05737-5, 2021a.
1381   Del Rio Amador, L., and Lovejoy, S., Long-range Forecasting as a Past Value Problem:
1382   Untangling Correlations and Causality with scaling, *Geophys. Res. Lett.*, 1-12 doi:
1383   10.1029/2020GL092147, 2021b.
1384   Dijkstra, H., *Nonlinear Climate Dynamics*, 357 pp., Cambridge University Press, 2013.
1385   Franzke, C., and O'Kane, T. (Eds.), *Nonlinear and Stochastic Climate Dynamics*,
1386   Cambridge University Press, Cambridge, 2017.
1387   Gripenberg, G., and Norros, I., On the Prediction of Fractional Brownian Motion *J. Appl.*
1388   *Prob.*, *33*, 400-410, 1996.
1389   Hasselmann, K., Stochastic Climate models, part I: Theory, *Tellus*, *28*, 473-485, 1976.
1390   Hebert, R. (2017), A Scaling Model for the Forced Climate Variability in the
1391   Anthropocene, MSc thesis, McGill University, Montreal.
1392   Hébert, R., Lovejoy, S., and Tremblay, B., An Observation-based Scaling Model for
1393   Climate Sensitivity Estimates and Global Projections to 2100, *Climate Dynamics*,
1394   *56*, 1105–1129 doi: doi.org/10.1007/s00382-020-05521-x, 2021.
1395   Herrmann, R., *Fractional Calculus: an Introduction for Physicists*, World Scientific,
1396   2011.
1397   Hilfer, R. (Ed.), *Applications of Fractional Calculus in Physics* World Scientific, 2000.

1398   Hipel, K. W., and McLeod, A. I., *Time series modelling of water resources and*
1399   *environmental systems*, 1st edn. ed., Elsevier, 1994.
1400   IPCC, *Climate Change 2013: The Physical Science Basis. Contribution of Working Group*
1401   *I to the Fifth Assessment Report of the Intergovernmental Panel on Climate*
1402   *Change.*, Cambridge University Press: Cambridge, 2013.
1403   Jumarie, G., Stochastic differential equations with fractional Brownian motion inputs,
1404   *Int. J. Systems. Sci.*, *24*, 1113, 1993.
1405   Karczewska, A., and Lizama, C., Solutions to stochastic fractional relaxation equations,
1406   *Phys. Scr.*, *T136* 7pp doi: 10.1088/0031-8949/2009/T136/014030 2009.
1407   Kou, S. C., and Sunney Xie, X., Generalized Langevin Equation with Fractional Gaussian
1408   Noise: Subdiffusion within a Single Protein Molecule, *Phys. Rev. Lett.*, *93*, 4 doi:
1409   10.1103/PhysRevLett.93.180603, 2004.
1410   Lovejoy, S., What is climate?, *EOS*, *94, (1), 1 January*, p1-2, 2013.
1411   Lovejoy, S., A voyage through scales, a missing quadrillion and why the climate is not
1412   what you expect, *Climate Dyn.*, *44*, 3187-3210 doi: doi: 10.1007/s00382-014-
1413   2324-0, 2015a.
1414   Lovejoy, S., Using scaling for macroweather forecasting including the pause, *Geophys.*
1415   *Res. Lett.*, *42*, 7148–7155 doi: DOI: 10.1002/2015GL065665, 2015b.
1416   Lovejoy, S., The spectra, intermittency and extremes of weather, macroweather and
1417   climate, *Nature Scientific Reports*, *8*, 1-13 doi: 10.1038/s41598-018-30829-4,
1418   2018.
1419   Lovejoy, S., *Weather, Macroweather and Climate: our random yet predictable*
1420   *atmosphere*, 334 pp., Oxford U. Press, 2019a.
1421   Lovejoy, S., The Half-order Energy Balance Equation, Part 2: The inhomogeneous
1422   HEBE and 2D energy balance models, *Earth Sys. Dyn.*, *in press* doi:
1423   https://doi.org/10.5194/esd-2020-13, 2021a.
1424   Lovejoy, S., The Half-order Energy Balance Equation, Part 1: The homogeneous HEBE
1425   and long memories, *Earth Syst .Dyn. , (in press)* doi:
1426   https://doi.org/10.5194/esd-2020-12, 2021b.
1427   Lovejoy, S., *Weather, Macroweather and Climate: our random yet predictible*
1428   *atmosphere* Oxford U. press, 2019b.
1429   Lovejoy, S., and Schertzer, D., *The Weather and Climate: Emergent Laws and*
1430   *Multifractal Cascades*, 496 pp., Cambridge University Press, 2013.
1431   Lovejoy, S., Del Rio Amador, L., and Hébert, R., Harnessing butterflies: theory and
1432   practice of the Stochastic Seasonal to Interannual Prediction System (StocSIPS), ,
1433   in *Nonlinear Advances in Geosciences,* , edited by A. A. Tsonis, pp. 305-355,
1434   Springer Nature, 2017.
1435   Lovejoy, S., del Rio Amador, L., and Hébert, R., The ScaLIng Macroweather Model
1436   (SLIMM): using scaling to forecast global-scale macroweather from months to
1437   Decades, *Earth Syst. Dynam.*, *6*, 1–22 doi: www.earth-syst-
1438   dynam.net/6/1/2015/, doi:10.5194/esd-6-1-2015, 2015.
1439   Lovejoy, S., Procyk, R., Hébert, R., and del Rio Amador, L., The Fractional Energy
1440   Balance Equation, *Quart. J. Roy. Met. Soc. ,* 1–25 doi:
1441   https://doi.org/10.1002/qj.4005, 2021.
1442   Lutz, E., Fractional Langevin equation, *Physical Review E*, *64*, 4 doi:
1443   10.1103/PhysRevE.64.051106, 2001.

1444 Magin, R., Sagher, Y., and Boregowda, S., Application of fractional calculus in modeling
1445   and solving the bioheat equation, in *Design and Nature II*, edited by M. W. Collins
1446   and C. A. Brebbia, pp. 207-216, WIT Press, 2004.
1447 Mainardi, F., and Pironi, P., The Fractional Langevin Equation: Brownian Motion
1448   Revisited, *Extracta Mathematicae 10* 140—154, 1996.
1449 Mandelbrot, B. B., *The Fractal Geometry of Nature*, Freeman, 1982.
1450 Mandelbrot, B. B., and Van Ness, J. W., Fractional Brownian motions, fractional noises
1451   and applications, *SIAM Review*, *10*, 422-450, 1968.
1452 Mandelbrot, B. B., and Wallis, J. R., Computer Experiments with fractional gaussian
1453   noises: part 3, mathematical appendix, *Water Resour Res*, *5*, 260–267 doi:
1454   org/10.1029/WR005 i001p 00260, 1969.
1455 Mathews, J., and Walker, R. L., *Mathematical methods of Physics*, W. A. Benjamin, 1973.
1456 Metzler, R., and Klafter, J., The Random Walks Guide To Anomalous Diffusion: A
1457   Fractional Dynamics Approach, *Physics Reports*, *339*, 1-77, 2000.
1458 Newman, M., An Empirical Benchmark for Decadal Forecasts of Global Surface
1459   Temperature Anomalies, *J. of Clim.* , *26*, 5260-5269 doi: DOI: 10.1175/JCLI-D-
1460   12-00590.1, 2013.
1461 Nonnenmacher, T. F., and Metzler, R., Applications of fractional calculus techniques to
1462   problems in biophysics, in *Fractional Calculus in physics*, edited by R. Hilfer, pp.
1463   377-427, World Scientific, 2000.
1464 North, G. R., and Kim, K. Y., *Energy Balance Climate Models*, 369 pp., Wiley-VCH, 2017.
1465 Oldham, K. B., Diffusive transport to planar, cylindrical and spherical electrodes, *J
1466   Electroanal Chem Interfacial Electrochem.*, *41*, 351–358, 1973.
1467 Oldham, K. B., and Spanier, J., A general solution of the diffusion equation for semi
1468   infinite geometries, *J Math Anal Appl 39*, 665–669, 1972.
1469 Palma, W., *Long-memory time series*, Wiley, 2007.
1470 Palmer, T. N., and Williams, P. (Eds.), *Stochastic physics and Climate models*, 480 pp.,
1471   Cambridge University PRess, Cambridge, 2010.
1472 Papoulis, A., *Probability, Random Variables and Stochastic Processes*, Mc Graw Hill,
1473   1965.
1474 Penland, C., A stochastic model of IndoPacific sea surface temperature anomalies
1475   *Physica D*, *98*, 534-558, 1996.
1476 Penland, C., and Magorian, T., Prediction of Nino 3 sea surface temperatures using
1477   linear inverse modeling, *J. Climate*, *6*, 1067–1076, 1993.
1478 Podlubny, I., *Fractional Differential Equations*, 340 pp., Academic Press, 1999.
1479 Procyk, R. (2021), The Fractional Energy Balance Equation: the Unification of
1480   Externally Forced and Internal Variability, MSc thesis, 111 pp, McGill University,
1481   Montreal, Canada.
1482 Procyk, R., Lovejoy, S., and Hébert, R., The Fractional Energy Balance Equation for
1483   Climate projections through 2100, *Earth Sys. Dyn. Disc.*, *under review* doi:
1484   org/10.5194/esd-2020-48 2020.
1485 Rypdal, K., Global temperature response to radiative forcing: Solar cycle versus
1486   volcanic eruptions, *J. Geophys. Res.*, *117*, D06115 doi: 10.1029/2011JD017283,
1487   2012.

Rypdal, K., Global warming projections derived from an observation-based minimal model, *Earth Syst. Dynam. Discuss.*, *6*, 1789-1813 doi: 10.5194/esdd-6-1789-2015, 2015.

Sardeshmukh, P., Compo, G. P., and Penland, C., Changes in probability assoicated with El Nino, *J. Climate*, *13*, 4268-4286, 2000.

Sardeshmukh, P. D., and Sura, P., Reconciling non-gaussian climate statistics with linear dynamics, *J. of Climate*, *22*, 1193-1207, 2009.

Schertzer, D., LarchevÍque, M., Duan, J., Yanovsky, V. V., and Lovejoy, S., Fractional Fokker-Planck equation for nonlinear stochastic differential equation driven by non-Gaussian Levy stable noises, *J. of Math. Physics*, *42*, 200-212, 2001.

Schiessel, H., Friedrich, C., and Blumen, A., Applications to problems in polymer physics and rheology, in *Fractional Calculus in physics*, edited by R. Hilfer, pp. 331-376, World Scientific, 2000.

Sellers, W. D., A global climate model based on the energy balance of the earth-atmosphere system, *J. Appl. Meteorol.*, *8*, 392-400, 1969.

Sierociuk, D., Dzielinski, A., Sarwas, G., Petras, I., Podlubny, I., and Skovranek, T., Modelling heat transfer in heterogeneous media using fractional calculus, *Philos. Trans. R. Soc. A Math. Phys. Eng. Sci.* , *371: 20120146* doi: org/10.1098/rsta.2012.0146, 2013.

van Hateren, J. H., A fractal climate response function can simulate global average temperature trends of the modern era and the past millennium, *Clim. Dyn.* , *40*, 2651 doi: https://doi.org/10.1007/s00382-012-1375-3, 2013.

Vojta, T., Skinner, S., and Metzler, R., Probability density of the fractional Langevin equation with reflecting walls, *Phys. Rev. E 100,* , 042142 doi: 10.1103/PhysRevE.100.042142, 2019.

Watkins, N., Fractional Stochastic Models for Heavy Tailed, and Long-Range Dependent, Fluctuations in Physical Systems, in *Nonlinear and Stochastic Climate Dynamics*, edited by C. Franzke and O. K. T., pp. 340-368, Cambridge University Press, 2017.

Watkins, N., chapman, s., Klages, R., Chechkin, A., Ford, I., and stainforth, d., Generalised Langevin Equations and the Climate Response Problem, *Earth and Space Science Open Archive* doi: doi:10.1002/essoar.10501367.1, 2019.

Watkins, N. W., Chapman, S. C., Chechkin, A., Ford, I., Klages, R., and Stainforth, D. A., On Generalized Langevin Dynamics and the Modelling of Global Mean Temperature, *arXiv:2007.06464v1*, *[cond-mat.stat-mech]* 2020.

West, B. J., Bologna, M., and Grigolini, P., *Physics of Fractal Operators*, 354 pp., Springer, 2003.

Ziegler, E., and Rehfeld, K., TransEBM v. 1.0: Description, tuning, and validation of a transient model of the Earth's energy balance in two dimensions, *Geosci. Model Devel. Disc.* doi: https://doi.org/10.5194/gmd-2020-237, 2020.